8-2016

Efficient Method for Calculations of Ro-vibrational States in Triatomic Molecules Near Dissociation Threshold: Application to Ozone

Alexander Teplukhin
Marquette University

Dmitri Babikov
Marquette University, dmitri.babikov@marquette.edu

Efficient method for calculations of ro-vibrational states in triatomic molecules near dissociation threshold: Application to ozone

Alexander Teplukhin and Dmitri Babikov[a)]
Department of Chemistry, Wehr Chemistry Building, Marquette University, Milwaukee, Wisconsin 53201-1881, USA

(Received 23 June 2016; accepted 5 September 2016; published online 20 September 2016)

A method for calculations of rotational-vibrational states of triatomic molecules up to dissociation threshold (and scattering resonances above it) is devised, that combines hyper-spherical coordinates, sequential diagonalization-truncation procedure, optimized grid DVR, and complex absorbing potential. Efficiency and accuracy of the method and new code are tested by computing the spectrum of ozone up to dissociation threshold, using two different potential energy surfaces. In both cases good agreement with results of previous studies is obtained for the lower energy states localized in the deep (~10 000 cm^{-1}) covalent well. Upper part of the bound state spectrum, within 600 cm^{-1} below dissociation threshold, is also computed and is analyzed in detail. It is found that long progressions of symmetric-stretching and bending states (up to 8 and 11 quanta, respectively) survive up to dissociation threshold and even above it, whereas excitations of the asymmetric-stretching overtones couple to the local vibration modes, making assignments difficult. Within 140 cm^{-1} below dissociation threshold, large-amplitude vibrational states of a floppy complex $O\cdots O_2$ are formed over the shallow van der Waals plateau. These are assigned using two local modes: the rocking-motion and the dissociative-motion progressions, up to 6 quanta in each, both with frequency ~20 cm^{-1}. Many of these plateau states are mixed with states of the covalent well. Interestingly, excitation of the rocking-motion helps keeping these states localized within the plateau region, by raising the effective barrier. *Published by AIP Publishing.* [http://dx.doi.org/10.1063/1.4962914]

I. INTRODUCTION

In recent years, a significant progress has been made in accurate *ab initio* calculations of global potential energy surfaces for small molecules that span the widest range of molecular geometries and energies, going from deep covalent wells (that accommodate stable molecular arrangements) toward the asymptotic range where much weaker van der Waals (vdW) forces dominate (and lead to formation of the weakly bound complexes or clusters) and all the way up to the formation/reaction channels (that describe reagents and products), and even above. Examples include surfaces for isomerization reactions of small polyatomic molecules,[1–3] for molecule-molecule interactions,[4,5] and very accurate surfaces for several triatomic and tetra-atomic molecules.[2,6] One example is a new and rather accurate potential energy surface (PES) of O_3 that has already been used recently to improve our understanding of the O atom exchange processes $O + O_2 \rightarrow O_2 + O$,[7–10] and of the ozone forming recombination reaction[11]

$$O + O_2 \Leftrightarrow O_3^* \xrightarrow{+\text{bath gas}} O_3.$$

Quantum mechanical description of molecular dynamics on such global potential energy surfaces is a very challenging task, since a broad range of molecular geometries is involved that calls for very large grids or basis sets in multiple dimensions, which translates into large matrices and very significant (often unaffordable) numerical cost of calculations. Relevant computational methodologies have been developed for molecular reaction dynamics in small polyatomic systems based on DVR techniques.[12–14] Those methods are able to cover a wide range of molecular geometries from reagents to products, but are focused exclusively on construction of a state-to-state transition matrix in the asymptotic region, bypassing calculations of the individual quantized states and their wave functions through the interaction region. In principle, such states and their wave functions could be determined using the FBR methods developed for calculations of bound rotational-vibrational states of the molecules,[15–17] but those methods become prohibitively expensive near the dissociation/reaction threshold where the PES "opens up" toward the entrance/exit channels. Therefore, a class of molecular dynamics problems that requires determination of energies and wave functions of ro-vibrational states close to dissociation threshold (and scattering resonances above it) represents a significant challenge.

One example of this sort is the above-mentioned recombination reaction that forms ozone. The process starts at energies *above* the dissociation threshold, where the thermal collisions of O and O_2 populate scattering resonances O_3^*. Those represent highly excited ro-vibrational states of O_3 and should be characterized by their energies, widths, and wave functions that determine the rates of their population, spontaneous decay, and quenching (by bath gas collisions) onto the bound states of O_3 somewhat *below* dissociation

a)Author to whom correspondence should be addressed. Electronic mail: dmitri.babikov@mu.edu

threshold. In order to treat these processes, we devised a method that combines some elements typical to the quantum reactive-dynamics calculations, with some other elements more typical to the multi-dimensional bound-states calculations. The resultant approach is efficient and fills the gap in computational methodology discussed above.

Namely, for description of vibrational motion in O_3 our approach employs the adiabatically adjusting principal-axis hyper-spherical coordinates[18,19] that contain only one dissociative degree of freedom (hyper-radius ρ) and two bound-like degrees of freedom (hyper-angles θ and φ). In order to reproduce efficiently the delocalized wave functions at energies near dissociation threshold, we combine the sequential diagonalization-truncation procedure to construct FBR in θ and φ with a variable-step DVR grid along ρ, optimized based on the value of local de-Broglie wavelength, that adjusts to the shape of the PES. Widths of resonances are obtained by introducing a complex absorbing potential along ρ in the asymptotic part of the PES. Symmetry of O_3 states is described by the coordinate φ, and is used to further simplify the calculations.

In our recent publication[11] we have already applied this method to compute energies and widths of relevant scattering resonances O_3^* for rotationally excited ozone molecules up to $J = 60$ and, based on those data, we derived the recombination rate coefficient for ozone formation, as well as its temperature and pressure dependencies. Good comparison with the available experimental data was obtained. In this second (more methodological) paper we present all details of our approach, since it is general and can be readily applied to several other important triatomic molecules, such as S_3,[20,21] SO_2,[22] NO_2,[23] and CO_2.[24] In order to conduct a rigorous benchmark study, we compute the spectrum of vibrational states in O_3 up to dissociation threshold using two different potential energy surfaces and compare our results against results available in the literature, computed by other groups for non-rotating molecule, $J = 0$. Then, we focus on an energy window of 600 cm^{-1} just below the threshold, since in the recently published kinetics study[11] we found that this part of the vibrational spectrum plays the most important role in the recombination process that forms ozone. Properties of these highly excited and delocalized vibrational states are explored and reported in great detail, including analysis of three-dimensional wave functions and their assignments.

II. THEORY

A. Hamiltonian operator in hyper-spherical coordinates

As initially derived by Johnson,[25] the total rotational-vibrational Hamiltonian operator for a triatomic system in hyper-spherical coordinates can be written in the form of $\hat{H} = \hat{T}_{vib} + \hat{V}_{rot} + \hat{T}_{cor} + \hat{V}_{pot}$, where the following notations are introduced:

$$\hat{T}_{vib} = -\frac{\hbar^2}{2\mu}\left\{\frac{1}{\rho^5}\frac{\partial}{\partial\rho}\rho^5\frac{\partial}{\partial\rho} + \frac{4}{\rho^2} \times \left[\frac{1}{\sin(2\theta)}\frac{\partial}{\partial\theta}\sin(2\theta)\frac{\partial}{\partial\theta} + \frac{1}{\sin^2\theta}\frac{\partial^2}{\partial\varphi^2}\right]\right\}, \quad (1)$$

$$\hat{V}_{rot} = \frac{1}{\mu\rho^2}\left[\frac{\hat{J}_x^2}{1+\sin\theta} + \frac{\hat{J}_y^2}{2\sin^2\theta} + \frac{\hat{J}_z^2}{1-\sin\theta}\right], \quad (2)$$

$$\hat{T}_{cor} = \frac{4i\hbar\cos\theta\,\hat{J}_y}{2\mu\rho^2\sin^2\theta}\frac{\partial}{\partial\varphi}. \quad (3)$$

Here $\hat{T}_{vib}$ is the kinetic energy operator for vibrational coordinates ρ, θ and φ, while $\hat{V}_{pot} = V_{pot}(\rho,\theta,\varphi)$ stands for the potential energy surface, $\hat{V}_{rot}$ represents centrifugal energy due to the overall rotation of the system, $\hat{T}_{cor}$ is the rotation-vibration (Coriolis) coupling term. Usual Euler angles α, β, and γ are used to describe rotational motion of the molecule. The body-fixed reference frame is defined by three principal axes of inertia, with axis z chosen according to Pack: it is a symmetry axis of an associated prolate symmetric-top, which minimizes couplings between different components of total angular momentum.[18] The overall volume element is $d^6\upsilon = {}^1/_8\rho^5\sin\theta\cos\theta\sin\beta\,d\rho\,d\theta\,d\varphi\,d\alpha\,d\beta\,d\gamma$. Since the normalized Wigner functions are used for expansion of the rotational wave function, $\tilde{D}^J_{KM}(\alpha,\beta,\gamma) = \sqrt{(2J+1)/8\pi^2}\cdot D^J_{KM}(\alpha,\beta,\gamma)$, analytic integration over the rotational degrees of freedom leads to the volume element $d^3\upsilon = {}^1/_8\rho^5\sin\theta\cos\theta\,d\rho\,d\theta\,d\varphi$.

In this or very similar forms, the hyper-spherical coordinates have been employed over the years by several groups, due to simplicity of the kinetic energy operator and ro-vibrational decoupling, and also due to convenience of describing molecular symmetry when identical atoms are involved. Most notable contributions were made by Parker, Pack and their co-workers,[13,18] by Kuppermann[26] and co-workers, more recently by Kendrick and co-workers,[15,17,27] by Kokoouline and Greene,[28–30] and also by several other independent followers.[31–33] The applications include both the reactive-scattering processes[13,17,18] and the bound-state calculations.[15,27,31–33]

In the past, several users made slight modifications to these hyper-spherical coordinates, in order to make them more suitable for their particular applications. Examples can be found in the work of Johnson,[25] Whitnell and Light,[34] Parker and Pack,[18] and Kendrick *et al.*[17,27] Some of those proposed transformations were intended to simplify the kinetic energy operator over ρ, others to deal with singularity over θ, or to enforce the desired symmetry properties over φ. Our goal was to obtain the simplest possible form of the kinetic energy operator with the simplest volume element. We found that this can be achieved by the following transformation of the "old" vibrational wave function, say $\bar{\Psi}(\rho,\theta,\varphi)$, to its new form $\Psi(\rho,\theta,\varphi)$, as follows:

$$\Psi(\rho,\theta,\varphi) \leftarrow {}^1/_4\rho^{5/2}\sin^{1/2}(2\theta)\,\bar{\Psi}(\rho,\theta,\varphi). \quad (4)$$

Then, the Hamiltonian operator acting onto this transformed wave function can be written as $\hat{H} = \hat{T}_{vib} + \hat{V}_{rot} + \hat{T}_{cor} + \hat{V}_{pot} + \hat{V}_{ext}$ where, instead of Eq. (1), a new expression is obtained for the vibrational kinetic energy operator

$$\hat{T}_{vib} = -\frac{\hbar^2}{2\mu}\left[\frac{\partial^2}{\partial\rho^2} + \frac{4}{\rho^2}\left(\frac{\partial^2}{\partial\theta^2} + \frac{1}{\sin^2\theta}\frac{\partial^2}{\partial\varphi^2}\right)\right], \quad (5)$$

and a new potential-like "extra" term is introduced

$$\hat{V}_{ext} = -\frac{\hbar^2}{2\mu\rho^2}\left[\frac{1}{4} + \frac{4}{\sin^2 2\theta}\right]. \quad (6)$$

We see that now the kinetic energy operator has the simplest form, with only three second derivatives along each ρ, θ, and φ. If the wave function is defined on a 3D-grid of points (direct-product DVR), the kinetic energy operator along each coordinate is trivially applied by Fourier-transforming the wave function to momentum representation, multiplying each point of it by $P^2/2\mu$, and Fourier-transforming it back to the coordinate representation (see, for example, Ref. 35). The additional potential term V_{ext} of Eq. (6) is simply added to the potential energy surface $V_{pot}(\rho,\theta,\varphi)$ and does not require any extra effort, since the potential energy operator is diagonal in the DVR representation. Furthermore, the volume element is now trivial: $d^3\upsilon = d\rho\, d\theta\, d\varphi$.

Interestingly, that while this work was in progress, we learned that we were not the first to discover this way of simplifying the hyper-spherical Hamiltonian operator. We found that this transformation was already discussed by Billing, in his book on the approximate quantum classical theory,[36] but was not applied to any real system.

B. Angular momentum decoupling approximation

In hyper-spherical coordinates the coupling between vibrational and rotational coordinates (the Coriolis coupling) is described by one cross-term in the Hamiltonian operator, $\hat{T}_{cor}$, Eq. (3), which contains both the rotational operator $\hat{J}_y$ and the vibrational operator $\partial/\partial\varphi$. If needed, the action of this term onto wave function $\Psi(\rho,\theta,\varphi)$ can be rigorously evaluated.[18] Typically, the value of Coriolis coupling is small, but it leads to linear growth of the Hamiltonian matrix size for $J > 0$, and quadratic growth of the numerical effort. For this reason, it is practical (and is often justified) to neglect this cross-term. Parker and Pack named this simplification the centrifugal-sudden approximation.[18] It is equivalent to the symmetric-top rotor assumption, also known as K-conserving approximation, since Hamiltonian operator of the symmetric-top rotor does not have such cross-term, and since projection K of angular momentum J onto symmetry axis of the rotor is conserved, making K a good quantum number.

Using this symmetric-top model, the Hamiltonian operator takes the simplest form $\hat{H} = \hat{T}_{vib} + V$, where all the potential terms are combined: $V = V_{pot} + V_{sym} + V_{ext}$, and the approximate centrifugal potential is given by

$$V_{sym} = \bar{A}\hbar^2 J(J+1) + (C - \bar{A})\hbar^2 K^2. \quad (7)$$

Here $\bar{A}$ and C are rotational constants of a symmetric top, with $\bar{A}$ being the approximate one, computed as average of two smaller rotational constants, A and B, of an asymmetric top: $\bar{A} = (A + B)/2$. Exact instantaneous values of the rotational constants in the hyper-spherical coordinates, according to Eq. (3), are defined as $A^{-1} = \mu\rho^2(1 + \sin\theta)$, $B^{-1} = 2\mu\rho^2 \sin^2\theta$ and $C^{-1} = \mu\rho^2(1 - \sin^2\theta)$. Note that the centrifugal potential of Eq. (7) is obtained from the exact expression of Eq. (3) by neglecting a piece that corresponds to the asymmetric-top rotor centrifugal potential $V_{asym} = (\hat{J}_x^2 - \hat{J}_y^2)(A - B)/2$. As it was emphasized by Parker and Pack[18] this simplification, together with neglect of the Coriolis coupling term, constitutes one single approximation, since both neglects are required in order to decouple the rotational and vibrational motions completely, in the hyper-spherical coordinates. Also, these rotational constants are those of a so-called *fluid* rotor, because the expression for B constant of *rigid* rotor does not contain $\sin^2\theta$.[18]

For example, for an ozone molecule in its equilibrium configuration the values of rotational constants are $A\hbar^2 = 0.45\ \text{cm}^{-1}$, $B\hbar^2 = 0.66\ \text{cm}^{-1}$, and $C\hbar^2 = 3.56\ \text{cm}^{-1}$, which makes it very close to a prolate symmetric-top rotor. For this reason, the K-conserving approximation has been used in the past in several studies of ozone spectra and dynamics,[35,37] and was also adopted in our recent work.[11] Within this approximation, calculations of vibrational states are carried out independently for different values of K, such that $K < J$, for each $J > 0$. In our recent study of recombination kinetics[11] we showed that significant contributions to the rate of ozone formation are made by states with moderate rotational excitations, in the range $8 \le J \le 38$, where this approximation is still expected to work reasonably well. The contribution of states with $J > 40$ was found to be small.

In the dissociation limit, when $\rho \to \infty$ and $\theta \to \pi/2$, the rotational constants A, B, and $\bar{A}$ vanish, while $C^{-1} \to 2\mu_{O_2} r^2 \sin^2\Theta$, showing dependence on the reduced mass of O_2 and Jacobi coordinates r and Θ. For T-shape configuration $\Theta = \pi/2$ and the equilibrium distance $r = r_e = 2.282\ a_0$, the value of C approaches the rotational constant of O_2, which is $1.44\ \text{cm}^{-1}$.

It should be stressed that in the hyper-spherical coordinates, also called adiabatically adjusting principal-axis hyper-spherical (APH) coordinates, symmetry axis of the approximate symmetric-top rotor is always the principal-axis of inertia a (pointing along vector **Q** as defined by Parker and Pack[18]) for any instantaneous molecular configuration,[38,39] and K is always a projection of **J** onto this axis, $K = K_a$. This choice minimizes Coriolis coupling[38] and makes the symmetric-top rotor approximation most accurate.[40] Note, however, that this is not automatically the case in other coordinates. For example, using Jacobi coordinates with R-embedding,[38] K is a projection of **J** onto the Jacobi vector **R**, and the values of rotational constants A, B, and C are defined relative to **R**. Although **R** becomes close to the principal-axis of inertia a in the asymptotic range (as $R \to \infty$), it should be realized that **R** deviates from a quite substantially when molecular geometry is close to the equilibrium configuration, making Coriolis coupling significant. One known way to fix this problem is to use the adiabatic-rotation (AR) approximation of Bowman,[40] that expresses rotational energy through the principal axis of inertia, rather than Jacobi vectors.

C. Direct-product basis set

In quantum mechanics, two most frequently used mathematical representations of wave function are the

finite basis representation (FBR) and the discrete variable representation (DVR).[41] In the FBR, wave function for the ith state is expanded over a basis set $\Phi_n(x)$, $1 \le n \le N$,

$$\Psi^{(i)}(x) = \sum_{n=1}^{N} a_n^{(i)} \Phi_n(x). \tag{8}$$

In the DVR, in contrast, a wave function is numerically approximated by a set of values at the points x_n of the grid

$$\Psi_n^{(i)} = \Psi^{(i)}(x_n). \tag{9}$$

Despite this difference, DVR can be thought of as a special case of FBR, where basis functions $f_n(x)$ are localized at the points of the grid

$$\Psi^{(i)}(x) = \sum_{n=1}^{N} b_n^{(i)} f_n(x), \tag{10}$$

$$f_n(x) = \begin{cases} 1, & x = x_n, \\ 0, & x \ne x_n. \end{cases} \tag{11}$$

Now consider a two-dimensional problem, with Hamiltonian operator $\hat{H} = \hat{T}_x + \hat{T}_y + V(x, y)$ and wave function represented as a *direct product* (of DVR or FBR) basis function for each dimension

$$\Psi^{(i)}(x, y) = \sum_{n=1}^{N} \sum_{m=1}^{M} a_{nm}^{(i)} \Phi_n(x) \Lambda_m(y). \tag{12}$$

This representation has $S = N \times M$ two-dimensional basis functions and the same number of expansion coefficients $a_{nm}^{(i)}$. The size of the Hamiltonian matrix is $S \times S$. Structurally, it consists of N^2 square blocks (x-blocks) labeled by n. Each block contains $M \times M$ elements (y-elements).

The advantage of this direct-product approach is its simplicity: the same basis set $\Lambda_m(y)$ for the coordinate y is used through the entire range of the coordinate x. Consequently, the same $M \times M$ matrix elements of the operator $\hat{T}_y$ are replicated over the entire matrix, in each x-block (see Fig. 1, top panel),

$$H_{nm,n'm'} = \langle n\, m | \hat{H} | n' m' \rangle = \delta_{m,m'} (\hat{T}_x)_{nn'} + \delta_{n,n'} (\hat{T}_y)_{mm'} + V_{nm,n'm'}. \tag{13}$$

The disadvantage of the direct-product approach is the large size of the basis set. Indeed, since exactly the same basis set $\Lambda_m(y)$ is going to be used at all (different) values of the coordinate x, this basis set must be *globally* good, which in practice means—rather large. Same applies to the basis set $\Phi_n(x)$, to be employed at all values of coordinate y. Thus, both N and M are expected to be large numbers, leading, in turn, to a large size of the resultant Hamiltonian matrix, which also increases rapidly with the addition of new coordinates. Namely, for a three-dimensional problem the size of the Hamiltonian matrix constructed using the direct-product FBR would be $S = N \times M \times L$, with L representing the number of basis functions for coordinate z (also large).

For example, we tried the direct-product DVR in hyperspherical coordinates ρ, θ, and φ to compute vibrational states of ozone. We found that for the states localized in the main

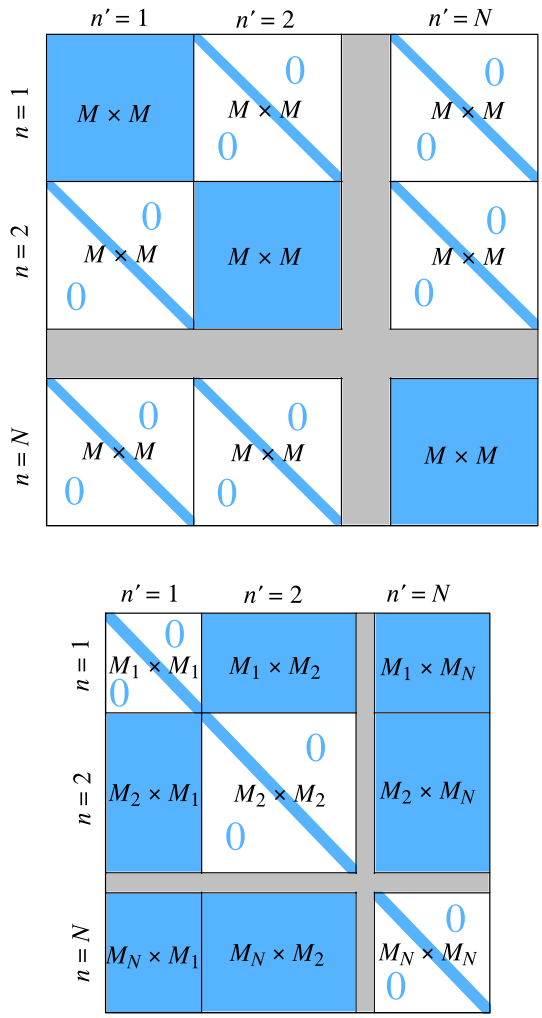

FIG. 1. Structure of Hamiltonian matrices constructed using the direct-product basis (top panel) and the sequential diagonalization-truncation approach (bottom panel). All elements of blue blocks are non-zero, while white blocks are already diagonal, with non-zero elements shown by the blue stripe. Note that all blocks of the first matrix have the same size and are squared, while all blocks of the second matrix are different and are smaller, $M_n \le M$, which results in a much smaller matrix size.

(covalent) well of ozone (not quite up to dissociation limit, just up to the van der Walls plateau, see below), a grid of $64 \times 64 \times 64$ equidistant points is sufficient for reasonably accurate results. This corresponds to the direct-product matrix size of almost $S = 3 \cdot 10^5$. But, such grid only covers a limited range of the hyper-radius, $3.3 \le \rho \le 6.0\ a_0$. Expanding this grid up to $\rho_{\max} = 15.0\ a_0$ (needed for calculations of all the bound states, including delocalized van der Waals states) would require $N = 280$ points along ρ, assuming the same step-size. This would lead to the matrix size of more than $S = 10^6$. Moreover, it appears that in the asymptotic range of the hyper-radius the PES is very tight, which requires a much denser grid, compared to the covalent well. For example, we found that at around $\rho_{\max} = 15\ a_0$ we need around $M = 280$ points for θ and $L = 400$ points for φ. Since the direct-product grid must be the same everywhere, one should use the $280 \times 280 \times 400$ grid, with the matrix size on the order of $S = 3 \cdot 10^7$, which is computationally unaffordable.

D. Sequential diagonalization-truncation

The problems described above can be largely reduced by avoiding one universal basis set, and, instead, using different basis sets in different parts of the configuration space. Those could be optimized and made much smaller, *locally*, in order to reduce the size of the overall Hamiltonian matrix. In the literature this idea is called the sequential diagonalization-truncation technique.[42–44] It is readily integrated into the hyper-spherical coordinates using an efficient combined DVR/FBR approach, as described below.

Since the vibrational operator $\hat{T}_{vib}$ of the Hamiltonian can be naturally split into two parts, $\hat{H} = \hat{T}_\rho + \hat{T}_{\theta\varphi} + V(\rho,\theta,\varphi)$, where

$$\hat{T}_{\theta\varphi} = -\frac{2\hbar^2}{\mu\rho^2}\left(\frac{\partial^2}{\partial\theta^2} + \frac{1}{\sin^2\theta}\frac{\partial^2}{\partial\varphi^2}\right). \quad (14)$$

It is possible to formulate and solve, first, a two-dimensional eigenvalue problem for the hyper-angles θ and φ, at different values of the hyper-radius ρ, keeping it fixed. For example, at $\rho = \rho_n$ the two-dimensional Hamiltonian operator is $\hat{h}_n = \hat{T}_{\theta\varphi} + V_n(\theta,\varphi)$ and the corresponding Schrödinger equation is

$$\hat{h}_n\Lambda^n_m(\theta,\varphi) = \varepsilon^n_m\Lambda^n_m(\theta,\varphi). \quad (15)$$

Here $V_n(\theta,\varphi) = V(\theta,\varphi;\rho_n)$ represents a two-dimensional slice through θ and φ of the potential energy surface at $\rho = \rho_n$. Numerical solution of this equation gives a set of two-dimensional eigenfunctions $\Lambda^n_m(\theta,\varphi)$ and a spectrum of the corresponding eigenvalues ε^n_m, labelled by index m, for each considered ρ_n. Note that since hyper-angles θ and φ are "bound-like" degrees of freedom, the corresponding two-dimensional slices $V_n(\theta,\varphi)$ of the PES are always localized to a relatively small range in the (θ,φ)-space, as illustrated by Fig. 2 (upper frames). Thus, the eigenvalue problem is well defined and is relatively easy to solve. The corresponding eigenfunctions $\Lambda^n_m(\theta,\varphi)$ and eigenvalues ε^n_m are always real-valued, even at high energies (above dissociation threshold) and at large ρ (in the asymptotic region). To illustrate this, we presented in Fig. 2 five lowest-energy eigenfunctions $\Lambda^n_m(\theta,\varphi)$ for three representative values of ρ. Furthermore, Fig. 3 shows energy eigenvalues ε^n_m as a function of slice number n along ρ. Each vertical "column" of points represents the energy spectrum of the two-dimensional Hamiltonian operator $\hat{h}_n$ for one slice. The minimum-energy path along ρ is also shown in Fig. 3 (by red line), which reflects the shape of the PES and makes the local zero-point energy ε^n_0 evident. The density of points in a given slice reflects properties of potential energy surface $V_n(\theta,\varphi)$ at ρ_n. For example, in the slice $n = 33$ the spectrum is sparser than in its vicinity, which corresponds to higher frequency, consistent with tight transition state in this slice. Slice $n = 17$ passes through the minimum of the covalent well, $D_e = 9275$ cm^{-1} relative to the bottom of the dissociation channel, that corresponds to classical dissociation limit. Finally, slice $n = 64$ (last slice in Fig. 3) passes though the dissociation channel of the PES. Here we can see that quantum threshold is 794.51 cm^{-1} above the classical dissociation limit, which corresponds to zero-point

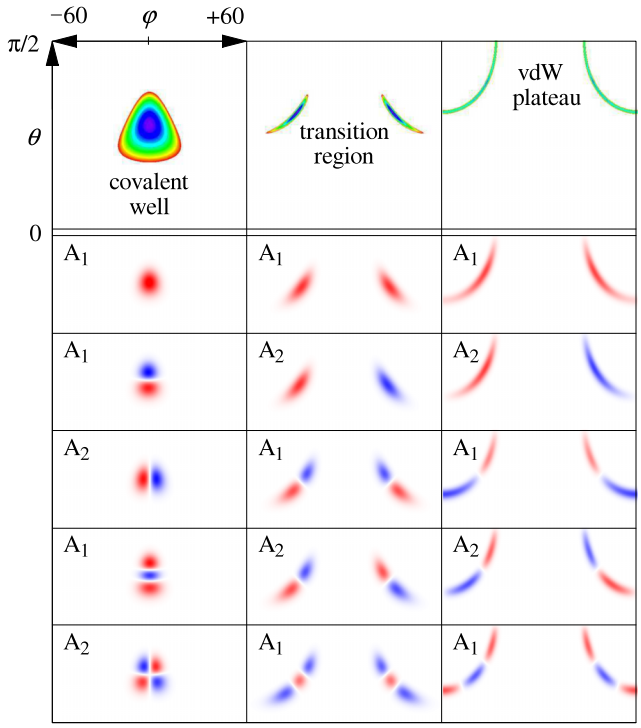

FIG. 2. Top row gives three representative two-dimensional slices $V_n(\theta,\varphi)$ of the PES: through the deep covalent well, through the transition region, and through the vdW plateau. The ranges of θ and φ are indicated in the upper left frame. Under each slice, the corresponding two-dimensional local basis set $\Lambda^n_m(\theta,\varphi)$ is presented (five lower energy functions). Positive and negative lobes of wave functions are shown in red and blue, respectively. Their nodal structure reveals excitations of the normal or local vibration modes and changes significantly between the slices, following the PES shape. Since potential is symmetric with respect to hyper-angle φ, the computed wave functions are either symmetric (A_1) or anti-symmetric (A_2).

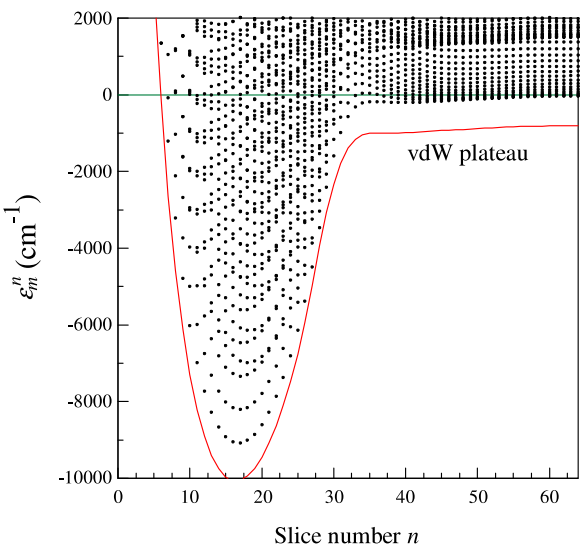

FIG. 3. Energies ε^n_m of two-dimensional eigenstates (black points) computed independently for each slice through the PES and plotted together as a function of slice number n. Only energies of A_1 states are shown, energies of A_2 states look similar. The minimum energy path for the PES is also shown for comparison (red line). Local vibrational zero-point energy is easily identified in each slice, as a distance between the lowest energy ε^n_0 and the minimum energy path. Asymptotically (to the right) the 2D-spectrum ε^n_m turns into the ro-vibrational spectrum of the diatomic fragment O_2. Dissociation threshold (green line) includes ZPE of O_2.

energy of $^{16}O_2$ in the state $v = 0$ and $j = 1$. The asymptotic form of $\Lambda_m^n(\theta,\varphi)$, as $\rho \to \infty$, is discussed in Appendix.

The two-dimensional solutions $\Lambda_m^n(\theta,\varphi)$ will be employed as locally optimal basis functions (at the next step, see below). Note that although the eigenstates $\Lambda_m^n(\theta,\varphi)$ for a given ρ_n form an orthonormal set, the functions determined at different slices, say $\Lambda_m^n(\theta,\varphi)$, $1 \le m \le M_n$ and $\Lambda_{m'}^{n'}(\theta,\varphi)$, $1 \le m' \le M_{n'}$ are not mutually orthogonal. In this case one can define the *overlap* matrix[18,45,46]

$$O_{nm,n'm'} = \int \Lambda_m^n \Lambda_{m'}^{n'} d\theta d\varphi. \tag{16}$$

The size of this matrix is $S \times S$, where $S = \sum_{n=1}^{N} M_n$ is the total number of two-dimensional functions determined and employed for the range of ρ. Structurally, the overlap matrix O contains N^2 blocks (ρ-blocks). Only the diagonal blocks are square, $M_n \times M_n$, and, by construction, are the identity matrices. The off-diagonal blocks of the overlap matrix are rectangular, with dimensions $M_n \times M_{n'}$. They contain couplings between different values of ρ.

The second step is to combine the local FBRs in θ and φ, with the DVR in ρ, by expressing the overall three-dimensional wave function as

$$\Psi^{(i)}(\rho,\theta,\varphi) = \sum_{n=1}^{N} \sum_{m=1}^{M_n} a_{nm}^{(i)} f_n(\rho) \Lambda_m^n(\theta,\varphi). \tag{17}$$

Importantly, size M_n of the local basis set $\Lambda_m^n(\theta,\varphi)$, $1 \le m \le M_n$, does not have to be the same for different values of ρ. Typically, it is minimal at $\rho \to 0$ (just a few functions in the repulsive region), is largest for the intermediate values of ρ (around 100 functions in the covalent well region), and is again small asymptotically as $\rho \to \infty$ (about a dozen functions in the channel region). In this representation, matrix elements of the total Hamiltonian operator $\hat{H}$ are computed as follows:

$$\begin{aligned} H_{nm,n'm'} &= \langle n\,m|\,\hat{H}\,|n'm'\rangle = \langle n\,m|\,\hat{T}_\rho\,|n'm'\rangle + \langle n\,m|\,\hat{T}_{\theta\varphi} + V\,|n'm'\rangle \\ &= \int \Lambda_m^n \Lambda_{m'}^{n'} d\theta d\varphi \times \int f_n \hat{T}_\rho f_{n'} d\rho + \int \Lambda_m^n \varepsilon_{m'}^{n'} \Lambda_{m'}^{n'} d\theta d\varphi \times \int f_n f_{n'} d\rho \\ &= O_{nm,n'm'} \times (\hat{T}_\rho)_{n,n'} + \delta_{m,m'}\delta_{n,n'}\varepsilon_m^n. \end{aligned} \tag{18}$$

Here $(\hat{T}_\rho)_{n,n'}$ is a square matrix, $N \times N$, of the kinetic energy operator in ρ,

$$\hat{T}_\rho = -\frac{\hbar^2}{2\mu}\frac{\partial^2}{\partial\rho^2}, \tag{19}$$

in the DVR basis (a grid of N points ρ_n). Equation (18) shows that the overall Hamiltonian matrix $H_{nm,n'm'}$ is easily constructed from the overlap matrix $O_{nm,n'm'}$ by multiplying each of its ρ-block by the corresponding element of the matrix $(\hat{T}_\rho)_{n,n'}$, and then adding to each diagonal element the corresponding value of two-dimensional energy ε_m^n. It is quite interesting that the PES $V(\rho,\theta,\varphi)$ does not show up in the final Eq. (18). All information about it, as well as the extra potential term V_{ext} and the rotational term V_{sym}, have already been encoded into the two-dimensional eigenvalues ε_m^n and the overlap matrix $O_{nm,n'm'}$ of two-dimensional eigenfunctions $\Lambda_m^n(\theta,\varphi)$.

Size of the Hamiltonian matrix is the same as that of the overlap matrix: $S \times S$, where $S = \sum_{n=1}^{N} M_n$. In practice, this means a significant reduction compared to the direct-product DVR in 3D. Local basis set $\Lambda_m^n(\theta,\varphi)$ at each ρ_n can be truncated based on a physical value of maximum energy in the problem, which gives one convenient convergence parameter for the entire problem: $\varepsilon_m^n \le E_{\text{cut}}$. In the ozone example considered in Sec. II C above, where the covalent well is $\sim 10^4$ cm^{-1} deep, we found that $E_{cut} = 7250$ cm^{-1} above dissociation limit is sufficient to obtain reliable results for all bound states below dissociation threshold, and also for scattering resonances at energies up to 1000 cm^{-1} above dissociation threshold. This seemingly large value of E_{cut} truncates basis sets down to only $M_n = 20$ functions in the asymptotic range of ρ, and around $M_n = 200$ functions in the covalent well region (see Fig. 3). At small ρ, in the repulsive range where all ε_m^n are above E_{cut}, we still keep 20 eigenvectors in the basis (10 of each symmetry, see below) as it was recommended by Carrington.[42–44]

Further speed up is obtained using symmetry of the vibrational states, as determined by the hyper-angle φ. For this, after the two-dimensional eigenfunctions $\Lambda_m^n(\theta,\varphi)$ have been computed, they should be analyzed and labeled as symmetric (A_1) or anti-symmetric (A_2) with respect to φ. Since those have no net overlap (due to cancellation of the integral), one can split each local basis set onto two separate basis sets of given symmetry: A_1 and A_2. Each is used independently, according to Eqs. (16)–(18), which reduces the size of Hamiltonian matrix even further, roughly by a factor of two, and produces three-dimensional solutions of different symmetries through two independent calculations.

This approach (in conjunction with optimized grid DVR for ρ, see Sec. II E) leads to the total basis and matrix size of only $S = 7 \cdot 10^3$, for each symmetry. Recall that this is instead of the direct-product matrix with the size around 10^7 (see example in Sec. II C above). Such a significant matrix reduction, by three orders of magnitude, is very appealing since the numerical cost of diagonalization algorithms scales as S^2 or S^3.

It is also instructive to mention the possibility of an adiabatic approximation, where the off-diagonal blocks of the overlap matrix $O_{nm,n'm'}$ are all neglected. This would lead, in the three-dimensional problem, to the Hamiltonian matrix that is automatically diagonal

$$H_{nm,n'm'} \approx \delta_{m,m'}\delta_{n,n'}(\hat{T}_\rho)_{n,n'} + \delta_{m,m'}\delta_{n,n'}\varepsilon^n_m. \quad (20)$$

Here, the diagonal elements of the kinetic energy operator in ρ are simply added to the values of two-dimensional energies in θ and φ. While useful in some cases, this approximation is expected to be rather rough in general. However, it should be recognized that a reasonably accurate approximation can be devised by neglecting not all, but some blocks of the overlap matrix. For example, those blocks that correspond to the values of ρ_n and $\rho_{n'}$ that are far apart may show negligible overlap anyway, and can be safely neglected.

The reason for efficiency of the sequential diagonalization-truncation approach discussed above is that each local basis set $\Lambda^n_m(\theta,\varphi)$ can be chosen relatively small, simply because its functions are perfectly suited to describe behavior of the overall wave-function near ρ_n. This is because $\Lambda^n_m(\theta,\varphi)$ are the local eigenfunctions, i.e., the best-possible functions, rather than some universal polynomials, or grids. Note, however, that this optimization concerns representation of a wave-function along θ and φ only, but not yet along ρ. Optimization of the grid $f(\rho_n)$ along ρ is discussed next.

E. Optimized grid DVR

Grid representation, or DVR, is a good choice for coordinate ρ, because this is a dissociative degree of freedom. When energy is high, the spectrum of states is continuous. Scattering resonances are important, that dissociate, exhibiting wave functions that expand far into the channels of the PES. In this regime the grid should expand to large values of ρ, but it does not have to be equally dense everywhere. It is clear physically that the grid should be denser over the deep covalent well, where the wave-function oscillates rapidly. However, in the asymptotic range of large ρ, where the dissociation channels are shallow, wave function does not oscillate much (e.g., see Fig. 9 below), and the grid does not have to be that dense.

Using this idea, the density of grid $f(\rho_n)$ along ρ can be optimized, locally, using the local value of de Broglie wavelength: $\lambda(\rho) = \pi/\sqrt{2\mu\,[E_{\max} - E_{\min}(\rho)]}$. Here $E_{\max}$ is a constant number, one characteristic maximum energy of the problem. We recommend $E_{\max} \approx 2kT$ at room temperature. In contrast, $E_{\min}$ is a variable of ρ, and is a local minimum possible energy of the system. In one-dimensional problems (diatomic molecules) this is simply the value of the PES, e.g., $E_{\min} = V(r)$.[47] In the multi-dimensional problems one can define the envelope potential for each coordinate, e.g., $E_{\min} = V_{\text{env}}(\rho)$, for example, by computing the minimum energy path along ρ. But this method does not take into account local zero-point energy of the system that, in principle, can change significantly along the reaction coordinate. We realized that it is best to define minimum energy as the ground state energy of the local two-dimensional eigenstates ε^n_m, which reflects the minimum energy path along ρ, but also takes the local zero-point energy into account (see Fig. 3). So, we use $E_{\min}(\rho) = \varepsilon_0(\rho)$. In practice it is constructed as a spline of the lowest energy values ε^n_0 determined on a trial grid of points ρ_n (that can be uniform and rather sparse everywhere).

Using the local de Broglie wavelength $\lambda(\rho)$, the local step-size for the variable grid is defined as[35]

$$\Delta\rho = \alpha\lambda(\rho)\Delta\xi = J\Delta\xi. \quad (21)$$

In this formulation, sometimes called grid mapping,[47,48] the equidistant (working) grid ξ_n with $\Delta\xi = 1$ is defined along the auxiliary unit-less coordinate ξ. The Jacobian of transformation is $J(\rho) = \alpha\lambda(\rho)$, where α is a constant compression factor ($\alpha < 1$ is used to make the grid denser than the minimal requirement $\alpha = 1$). In order to generate the optimal grid ρ_n, the differential equation $d\rho/d\xi = J(\rho)$ is solved numerically (e.g., by 4th-order Runge-Kutta method) with boundary condition $\rho = \rho_{\min}$ at $\xi = 0$, to determine the values of ρ_n at the points ξ_n. As it is often done, we place grid points in the middle of intervals, so, $\xi_1 = 0.5$ and ρ_1 is slightly larger than $\rho_{\min}$. Figure 4 gives an example of such variable-step grid. One can see that the density of points is much lower in the range of shallow van der Waals (vdW) plateau, and in the dissociation channel, compared to the region of deep covalent well. Grid density changes smoothly through the range of ρ. In the final calculations we used a denser grid, generated using $\alpha = 0.5$.

In fact, the physical optimized grid is only used for plotting the wave function (see Fig. 6), for all other purposes the working grid ξ_n is used. For example, applying the kinetic energy operator in ρ is done using the equidistant grid ξ_n, rather than a variable step-size grid ρ_n. The change of variable is taken into account using the Jacobian of transformation $J(\xi)$, not to confuse with total angular momentum

$$\hat{T}_\xi = -\frac{\hbar^2}{2\mu}\left(\frac{1}{J}\frac{\partial}{\partial\xi}\frac{1}{J}\frac{\partial}{\partial\xi}\right). \quad (22)$$

In order to keep the operator Hermitian and the matrix symmetric, a new wave function is introduced, with its

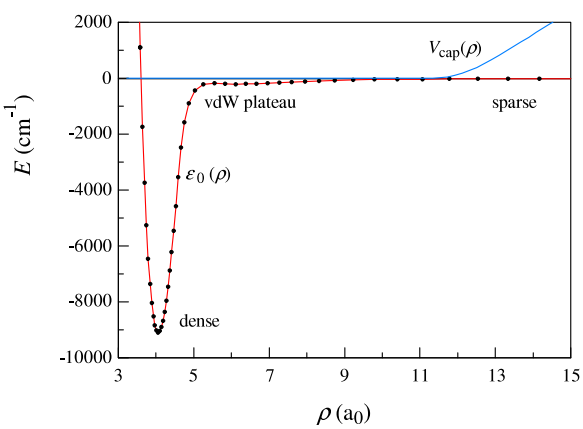

FIG. 4. Variable-step grid generated for the dissociative coordinate ρ (black points). The grid is dense in the covalent well, is sparser in the vdW plateau region, and is even sparser in the asymptotic range. The ground state value of local 2D energy $\varepsilon_0(\rho)$, used to generate this grid, is also shown (red line). The complex absorbing potential $V_{cap}(\rho)$ is shown in the asymptotic region (blue line).

corresponding operator

$$\tilde{\Psi}(\xi) = \sqrt{J(\xi)}\ \Psi(\rho), \tag{23}$$

$$\hat{T}_\xi = -\frac{\hbar^2}{2\mu}\left(\frac{1}{\sqrt{J}}\ \frac{\partial}{\partial\xi}\ \frac{1}{J}\ \frac{\partial}{\partial\xi}\ \frac{1}{\sqrt{J}}\right). \tag{24}$$

F. Calculations of resonance widths

Widths of scattering resonances, reported in Ref. 11, were computed by introducing into the range of large ρ values the complex absorbing potential in the analytic form suggested by Balint-Kurti,

$$V_{cap}(\rho) = -iA\exp\left(\frac{W}{\rho-\rho_c}\right), \tag{25}$$

with a set of parameters determined in our earlier paper:[35] $A = 10^4\,\mathrm{cm}^{-1}$, $\rho_c = 10.5\,a_0$, and $W = 6.5\,a_0$. It is important to realize that $V_{cap}(\rho)$ depends on the value of hyper-radius ρ only, and does not change through the two dimensional slice over θ and φ, which means that it does not affect two-dimensional solutions $\Lambda^n_m(\theta,\varphi)$ and the overlap matrix $O_{nm,n'm'}$, besides a constant shift $V_{cap}(\rho_n) = V^n_{\mathrm{cap}}$. So, introduction of the complex potential only affects the last step of our method, by changing the Hamiltonian matrix

$$H_{nm,n'm'} = O_{nm,n'm'} \times (\hat{T}_\xi)_{n,n'} + \delta_{m,m'}\delta_{n,n'}(\varepsilon^n_m + V^n_{\mathrm{cap}}). \tag{26}$$

This matrix has the same size S as in the real-valued case of Eq. (18), but it is non-Hermitian and exhibits complex eigenvalues $E - i\Gamma/2$. Note, however, that the two-dimensional solutions $\Lambda^n_m(\theta,\varphi)$ stay real functions in this formalism; complexity comes solely from the third dimension of the problem—the dissociative coordinate ρ. Distribution of resonance energies E and widths Γ for calculations with $0 < J < 60$, $K < J$, and their role in the recombination process that forms O_3 were discussed in detail in a recent paper.[11]

G. Notes

The approach we devised here has several things in common with previous studies where the hyper-spherical coordinates were employed. For example, it resembles the methods of Pack,[13,18] Kendrick,[15,17,27] and Kokoouline and Greene[28–30] in what concerns the consecutive treatment of, first, the hyper-angular degrees of freedom (θ,φ), and then, of the hyper-radius ρ. However, the standard approach is to use the coupled-channel (scattering) formalism for the hyper-radial coordinate, while we solve *the eigenvalue problem*. Typically, the goal of scattering calculations is to obtain the state-to-state transition matrix (e.g., for O + O_2 collisions), while our approach is better suited for calculations of the bound states and scattering resonances in O_3, using the *complex absorbing potential*. Traditionally, the CAP is used in conjunction with Jacobi coordinates, where a separate CAP has to be placed and tuned in each dissociation channel. In contrast, in the hyper-spherical coordinates a single CAP defined along the hyper-radius ρ takes care of all dissociative parts of the wave function, in all three channels. On the other hand, our formalism relies heavily on the idea of *sequential diagonalization truncation* proposed by Bačić and Light,[42–44] but this technique is normally applied to other types of coordinates (such as Jacobi), not the hyper-spherical coordinates. Finally, we use the adaptive grid along the hyper-radius ρ, and combine the DVR along ρ, with the FBR for (θ,φ), which is both practically convenient and numerically efficient.

We would like to note that during the editorial process it was brought to our attention that a very similar approach was recently developed by Kokoouline and co-workers.[46,49–51] They also use DVR in the hyper-spherical coordinates, and solve the complex-eigenvalue problem using the CAP. They use the abbreviation SVD for their method, which stands for *slow variable discretization* (meaning the hyper-radius ρ). Many components of our method are, indeed, the same. One methodological feature that we use, and they do not, is the sequential diagonalization-truncation technique, which makes calculations very efficient.

On the technical side we want to note that matrix diagonalizations were done in parallel using ScaLapack.[52] The kinetic energy operator is applied using FFT, which corresponds to periodic behavior for φ (Neumann boundary conditions), consistent with symmetries A_1 and A_2. For θ and ρ wave function vanishes at the ends of the grid, due to high potential energy. Two-dimensional eigenfunctions $\Lambda^n_m(\theta,\varphi)$ were obtained in two steps, using the same sequential diagonalization-truncation approach. Namely, we start with a 1D DVR in φ, which can be very dense, 400 points in the range $2\pi/3 \le \varphi \le 4\pi/3$, but causes no issues since 1D solutions are computationally cheap. Those are determined for each value of θ on the grid (280 points through $0.43 \le \theta \le \pi/2$), and for each ρ slice (86 optimally spaced points in the range $3.3 \le \rho \le 15.0\ a_0$). Those are truncated using E_{cut} (same value as reported above) retaining between 3 and 30 functions (of one symmetry), depending on the values of θ and ρ. These locally optimal and truncated 1D basis sets are used to set up the Hamiltonian matrix for a 2D problem in θ and φ, diagonalization of which gives $\Lambda^n_m(\theta,\varphi)$. Since 1D and 2D calculations are (typically) very fast, we use simple equidistant grids, but in principle, grid optimization in φ and θ can also be implemented, similar to what was done for ρ. Further fine-tuning can be done by adjusting the ranges of the grids in φ and θ, and the grid density, individually for different slices in ρ. Figure 2 clearly shows that the grids in φ and θ do not have to be the same at different values of ρ.

We conducted careful convergence studies making sure that the values of energies for scattering resonances in the window 400 cm^{-1} above dissociation threshold are obtained with accuracy better than 1 cm^{-1} (energies of the bound states are converged better than this). To summarize, our convergence parameters, all tested individually, include the number of points for DVR in φ, the number of points for DVR in θ, the density of optimized grid in ρ determined by $E_{\max}$ and α, the extent of the grid $[\rho_{\min},\rho_{\max}]$, and the value of energy cutoff E_{cut} (used for truncation of 1D FBR basis in φ during solution of the 2D-problem, and for truncation of 2D FBR basis in hyper-angles during solution of the 3D-problem). The final values of these parameters were given

throughout the text above, and will not be repeated again here. Note that this procedure bypasses common convergence studies of 2D energies ε_m^n, since only the final values of 3D energies matter. For scattering resonances, discussed in detail in the earlier paper,[11] we also checked the effect of absorbing potential (position, width, and steepness) on resonance lifetimes, making sure that convergence of the recombination rate coefficient, determined by these lifetimes, is close to 5%.

III. RESULTS AND DISCUSSIONS

As mentioned above, application of our method to calculations of scattering resonances above dissociation threshold for a broad range of rotational excitations ($0 < J < 60$) was reported in a recent paper.[11] Here, as a benchmark study of our method and new code, we compute the bound vibrational states of $^{16}O^{16}O^{16}O$ up to dissociation threshold for $J = 0$ and compare our results against results of another recently published paper,[11] where the standard approach (based on Jacobi coordinates) and a well-tested code were employed by another group. In the past similar calculations were carried out by several independent groups[53–55] using the older surface of ozone. The focus here is on the upper part of the spectrum, within 600 cm^{-1} below dissociation threshold, because we found that these vibrational states (bound in the $J = 0$ case) become scattering resonances when the rotational excitation ($J > 0$) lifts them above the dissociation threshold, where these states can be populated from the continuum through $O + O_2 \rightarrow O_3^*$, and can contribute to the recombination process, O_3^* (+bath gas) $\rightarrow O_3$.[11] Thus, it is necessary to have all these states accurately computed, analyzed, and assigned, if only possible. Dissociation limit is defined as electronic energy of $O + O_2$ asymptote on the PES, plus the ro-vibrational energy of O_2 in the lowest-energy physically allowed state ($v = 0, j = 1$), which is 794.51 cm^{-1} for $^{16}O^{16}O$. This number was determined by 1D calculations for a slice through the asymptotic range of the PES, using a very dense grid of DVR points.

A. Lower part of vibrational spectrum in the well

For completeness, we also report the spectrum of vibrational states at energies lower than our "target" window of 600 cm^{-1} below dissociation threshold. Due to space consideration, these are given in the supplementary material (Table S-I) and include 209 states, with the ground vibrational state at energy −8618.25 cm^{-1} below dissociation limit. The states are rigorously assigned by symmetry, A_1 for symmetric and A_2 for antisymmetric, and are also qualitatively assigned the normal mode quantum numbers (v_1, v_2, v_3) that correspond to symmetric stretch (breathing), bending, and asymmetric stretch, respectively. The normal mode assignment is done by visual inspection of the vibrational wave functions, and often is not entirely certain. One reason for this uncertainty is some *local-mode* character (due to the PES shape) mixed into the usually dominant normal-mode behavior. Such states are still assigned the normal mode quantum numbers in Table S-I, but are labelled by "LM." Several lower energy examples are states (2,0,2), (2,1,2), and (2,0,3). At higher energies the local-mode behavior becomes the main reason for uncertainty of the normal mode assignments, as one can see from Table S-I. The second reason is similarity of the symmetric stretch and asymmetric stretch frequencies, v_1 and v_3, that lead to similar energies of the states (v_1, v_2, v_3) and $(v_1 + 1, v_2, v_3 - 1)$. Such states have the same total number of quanta, but one quantum of asymmetric stretch is replaced by one quantum of symmetric stretch. In Table S-I these pairs are labelled by "P#" where number indicates the corresponding pair state. Lowest energy example of this sort is the pair of states (0,0,4) and (1,0,3), followed by the pair of (0,1,4) and (1,1,3), and then by (0,0,5) and (1,0,4). Such pairs are more common at lower energies.

In order to have a quantitative picture of the vibrational spectrum in this energy range, we tried to fit our computed spectrum by the standard Dunham expansion formula, that has 10 fitting parameters: three harmonic frequencies $(\omega_1, \omega_2, \omega_3)$, three intra-mode anharmonicities $(\Delta_1, \Delta_2, \Delta_3)$, three inter-mode anharmonicities $(\Delta_{12}, \Delta_{23}, \Delta_{31})$, and the well depth D. Results for four fits, using different number of computed states (60, 120, and 180 lower energy states) are summarized in Table I. We see that the value of symmetric stretch frequency ω_1 and its corresponding anharmonicity Δ_1 are less sensitive to the number of states included (compared to other parameters), the values of ω_1 and ω_3 are different only by ∼10 cm^{-1} (but are quite different from ω_2), and that the bending mode is the most harmonic ($\Delta_2 \sim 2$ cm^{-1}).

Although these fits are reasonable, they are not particularly responsive to all properties of the spectra, showing rather large standard deviations (up to ∼30 cm^{-1} in the case of 180 fitted states). Deviations of computed energies from the Dunham fit of 248 states (all the covalent well states, see below) are also given in Table S-I. We see that the bending mode states, even the highly excited ones, deviate little from the Dunham expansion. Examples are (0,10,0), (0,9,1), (1,9,0), (0,11,0), (0,10,1), and (1,10,0) that are within 10 cm^{-1} of the fit. Note that those are easily assignable states. In contrast, the largest deviations from the Dunham

TABLE I. Dunham expansion fitting coefficients (in cm^{-1}) for the vibrational spectrum of ozone.

	Number of states fitted			
	60	120	180	248[a]
ω_1	1127.5	1126.3	1128.6	1141.6
ω_2	712.2	717.3	723.1	739.2
ω_3	1111.8	1119.1	1134.9	1157.4
Δ_1	3.4	3.2	3.4	4.1
Δ_2	1.7	2.0	2.2	2.9
Δ_3	16.6	18.2	20.5	22.2
Δ_{12}	8.8	10.3	11.2	13.8
Δ_{13}	34.6	30.8	30.1	32.2
Δ_{23}	16.7	18.6	20.6	24.6
D	−10 075.9	−10 086.3	−10 107.9	−10 159.7
Std. dev.	10.0	18.7	30.8	52.1

[a]Including all states below vdW plateau of the PES.

fit are observed for states that are hard-to-assign in terms of the normal mode quantum numbers (which makes sense, since the Dunham expansion assumes normal mode behavior). Thus, the states with the local mode character present, labelled "LM" in Table S-I, often deviate from the Dunham fit by more than 100 cm^{-1}. They typically have fewer quanta of bending, but more stretching quanta, in particular the asymmetric-stretching that asymptotically correlates with the local-mode (dissociative) motion. Examples are states (2,0,5), (1,1,6), (1,3,5), (2,1,5), (2,0,6), and (2,3,4).

Importantly, we found much better agreement between our computed energies and the energies reported by Ndengué *et al.*[56] Deviations are presented in Table S-I and we see that they increase from only −0.08 cm^{-1} for the ground state at −8618.25 cm^{-1}, to about −1 cm^{-1} for the states at energies near −1000 cm^{-1}, and stay at that level for the upper states in Table S-I, up to energies −600 cm^{-1}. The difference is always negative and changes smoothly, which indicates some kind of a systematic, rather than random difference, more likely due to methodologies used, rather than the issue of convergence. Interestingly, the differences are slightly *smaller* for those hard to assign states (labeled by P# in Table S-I), relative to the other states in their vicinity. Overall, taking into account the difference of methods, coordinates, basis sets, etc., this level of agreement can be characterized as good.

As for state assignments, Ndengué *et al.*[56] provided assignments for the lowest 120 states only. Our assignments go much higher in energy, although, as it was discussed above, some of them are not entirely certain. But, for the lowest 120 states our assignment fully agrees with those of Ndengué *et al.*[56]

We want to mention that we also carried out calculations of vibrational states using the older PES for O_3, developed by Schinke and co-workers,[57] and compared our results with their results. They reported 185 bound states and, for the most part, our energies and assignments agreed with their results, with mean deviation of only 0.6 cm^{-1} through the entire spectrum, except several upper states where the assignment of Schinke was uncertain, and some of the states were missing. Note that Schinke carried out a detailed comparison of his spectrum against experimental results from the literature. He reported mean deviation of only 4 cm^{-1} between his computed and experimental spectra. This gives us even more confidence in our method and new code.

B. Upper part of vibrational spectrum in the well

Overall, we found 288 bound vibrational states for $J = 0$ ozone on the PES of Dawes, out of which 163 are symmetric (A_1) and 125 are antisymmetric (A_2). This agrees well with results of Ref. 56 where 160 symmetric and 125 antisymmetric states were reported. Figure 5 shows energy of vibrational states (both symmetries) as a function of state number in the window 600 cm^{-1} below dissociation threshold, which gives information about density of states in this important part of the spectrum. We see that the density of states is roughly constant in the range of energies from −600 cm^{-1} to roughly −140 cm^{-1}, with average spacing between the states of about 11.7 cm^{-1}. In the energy range from −140 cm^{-1} up to zero (dissociation threshold) the density is also constant, with average spacing of about 3.6 cm^{-1}. This pronounced transition occurs due to opening of the "shoulder" or "plateau" region of the PES that can accommodate additional vdW-type states. This region of the PES is seen on the minimum-energy path along ρ in Fig. 3, but is also reflected by two-dimensional energies ε_m^n in Fig. 3, and, in particular, by the ground state energy ε_0^n in Fig. 4.

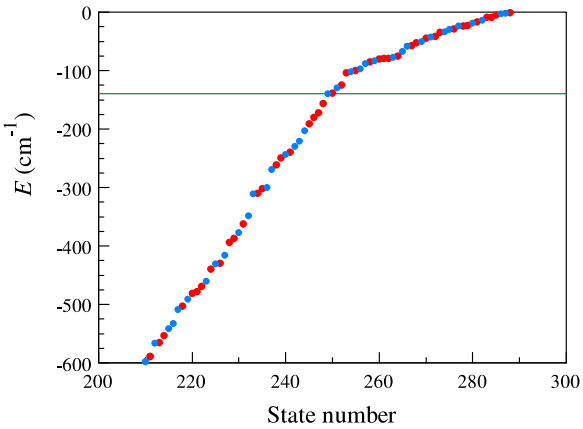

FIG. 5. Computed vibrational spectrum of ozone (energy vs. state number) in the window 600 cm^{-1} below dissociation threshold. States of symmetry A_1 and A_2 are indicated by red and blue points, respectively. Energy of the lowest vdW state at −139.8 cm^{-1} is shown by solid line. Slightly above that point, near the energy of the second vdW state at −103.5 cm^{-1} the density of states increases significantly, due to excitation of the local modes in the vdW plateau.

In this subsection we focus on the vibrational spectrum at energies between −600 cm^{-1} and −140 cm^{-1}, that has no vdW states. It contains states numbered 210 to 248, with properties summarized in Table II. As before, assignments of states in terms of the normal mode quantum numbers (v_1, v_2, v_3) are given, but only one-third of states in this energy range are clearly assignable. The local-mode character is strongly mixed into wave functions of the remaining two-thirds of states. For such states, marked by a superscript c in Table II, we give tentative assignments based on several factors, such as state energy and mode progression, in addition to visual analysis of vibrational wave function. The last column of Table II gives deviations of state energies from the Dunham expansion fit of all the covalent well states in the range from the ground vibrational state up to 140 cm^{-1} below dissociation threshold. Again, those states that are easily assignable show smaller deviations from the fit, while those that are hard to assign show larger deviations from the fit. Overall, based on absolute values of deviations from the fit, one can conclude the Dunham formula is not particularly useful in this energy range.

In this energy range the easily assignable states are those that have many quanta of bending and/or symmetric stretch, but no (or just a few) quanta of asymmetric stretch. This is easy to understand, since the large-amplitude asymmetric stretching motion correlates with dissociation of one bond, $O_3 \rightarrow O_2 + O$, that brings system to configuration space where the local-mode description of vibrations becomes appropriate. This leads to the appearance of the local-mode behavior in the vibrational wave functions and makes difficult (or even

TABLE II. Vibrational spectrum of ozone from 600 cm^{-1} below dissociation threshold up to vdW plateau.

#	E, cm^{-1}	Sym.	(v_1,v_2,v_3)[a]	δ[b] cm^{-1}
210	−597.8	A_2	(1,4,5)[c]	133.9
211	−589.3	A_1	(5,4,0)	−61.4
212	−566.0	A_2	(2,5,3)	44.7
213	−565.1	A_1	(0,4,6)[c]	−29.2
214	−552.9	A_1	(1,8,2)[c]	101.6
215	−541.8	A_2	(5,0,3)	−15.4
216	−532.8	A_2	(1,1,7)[c]	−60.1
217	−508.9	A_2	(0,8,3)[c]	−79.3
218	−502.3	A_1	(1,0,8)[c]	123.0
219	−490.7	A_2	(0,0,9)[c]	−12.6
220	−480.6	A_1	(0,12,0)	−4.2
221	−478.0	A_1	(7,1,0)	30.6
222	−469.4	A_1	(3,2,4)[c]	−61.1
223	−459.7	A_2	(0,3,7)[c]	61.0
224	−439.7	A_1	(2,4,4)[c]	117.9
225	−430.6	A_2	(5,3,1)	2.5
226	−429.4	A_1	(2,9,0)	−57.2
227	−415.9	A_2	(1,7,3)[c]	145.9
228	−393.6	A_1	(3,5,2)[c]	24.7
229	−386.5	A_1	(6,0,2)	−0.6
230	−377.0	A_2	(3,6,1)[c]	−193.9
231	−361.8	A_1	(2,7,2)[c]	241.8
232	−348.1	A_2	(4,2,3)[c]	−26.2
233	−311.0	A_2	(2,8,1)[c]	8.2
234	−309.4	A_1	(4,6,0)	−99.0
235	−301.9	A_1	(2,1,6)[c]	−156.9
236	−299.6	A_2	(0,11,1)	−20.9
237	−268.7	A_2	(3,4,3)[c]	100.7
238	−261.5	A_1	(0,2,8)[c]	57.2
239	−249.5	A_1	(1,3,6)[c]	−17.5
240	−243.2	A_2	(3,1,5)[c]	−69.8
241	−239.5	A_1	(6,3,0)	−10.6
242	−229.5	A_2	(4,5,1)[c]	24.5
243	−220.9	A_2	(7,0,1)	15.7
244	−202.9	A_2	(2,3,5)[c]	79.5
245	−191.0	A_1	(0,10,2)	33.8
246	−180.1	A_1	(5,2,2)[c]	−26.5
247	−172.1	A_1	(0,7,4)[c]	−236.1
248	−156.1	A_1	(4,4,2)[c]	153.5

[a]Assignment using normal-vibration modes.
[b]Deviation from the fit by Dunham expansion.
[c]Wave function exhibits some local-mode character, the assignment is approximate.

impossible) the assignment in terms of the normal modes. In contrast, neither bending nor symmetric stretching motion correlates with dissociation, which keeps even highly excited vibrations localized in the well region, and preserves the normal mode behavior.

Although it is clear that bending does not promote bond breaking, it may not be clear why the symmetric stretching motion does not lead to dissociation. This is so because stretching of two bonds simultaneously and in phase is not going to break one of them, while breaking two at the same time is impossible energetically.

So, among the easily assignable states in this energy range there are several dominantly symmetric stretching states, such as (8,0,0), (7,1,0), (7,0,1), (6,3,0), (6,0,2), and (5,0,3), there are several dominantly bending states, such as (0,12,0), (0,11,1), (0,10,2), (2,9,0), and (2,5,3), and there are several mixed states such as (5,4,0), (4,6,0), and (5,3,1). Figure 6 presents three-dimensional views of wave functions for all easily assignable states in this energy range. All of them are characterized by a relatively simple nodal structure and, although some of them show very significant spatial extent along the normal mode coordinate (e.g., very impressive bending progressions), neither of these functions extends into the dissociation channels.

In contrast to this behavior, Fig. 7 gives examples of wave functions for four states that are hard to assign.

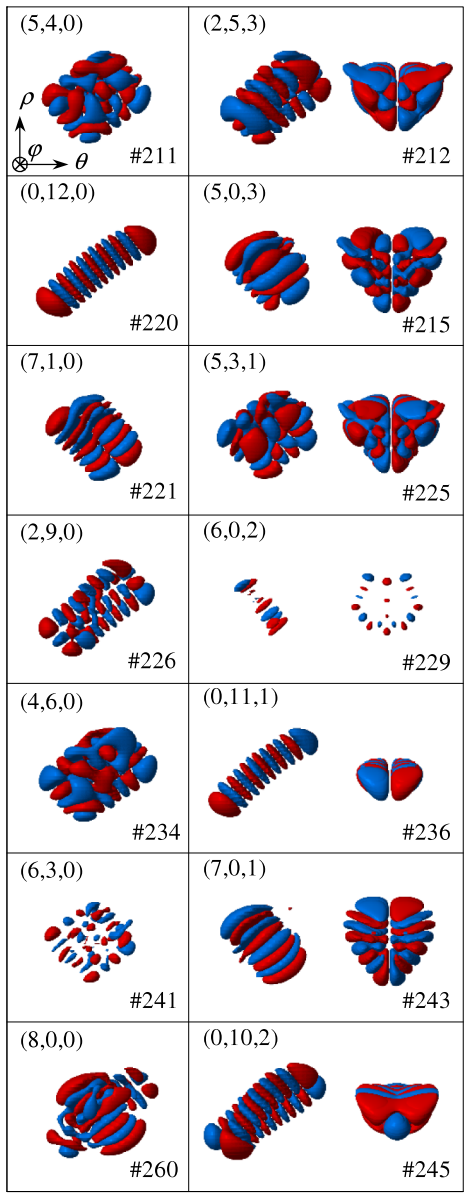

FIG. 6. Examples of easily assignable wave functions of ozone in the energy range below the vdW plateau. Positive and negative lobes of wave functions are plotted in red and blue, respectively, using the iso-value of $|\Psi| = 0.70$. Hyper-spherical system of coordinates is given in the upper left frame. Assignment by normal modes (v_1, v_2, v_3) and state number is given in the corners of each frame. Nodal structure of each wave function is readily identified, since these states are localized in the covalent well. States in the left column have no excitation in φ and thus only one (side) view is shown, while states in the right column have several excitation quanta in φ, so, in addition to the side view the second (front) view is presented.

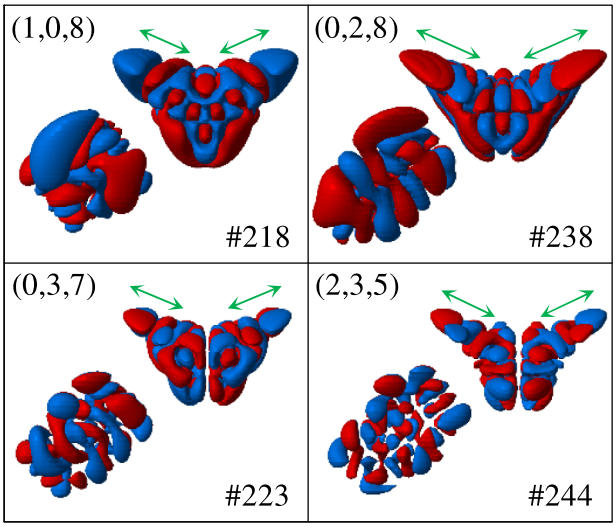

FIG. 7. Examples of hard-to-assign wave functions of ozone in the energy range below the vdW plateau. Labels, colors, and positions are the same as in Fig. 6. Due to significant excitation of asymmetric stretch ($v_3 \geq 5$) wave functions of these states extend significantly towards the dissociative channels of the PES, where the nodal structure reflects excitation of the local-mode vibrations (indicated by green arrows). Such states can be assigned only approximately, due to significant mixing of the normal and local vibration modes, in contrast to Fig. 6, where the states are localized, simple, and easily assignable.

All of them exhibit very significant excitation of the asymmetric stretching mode—five quanta and above. Their wave functions extend significantly into the dissociation channels, which is seen in Fig. 7 at two "wings" of the wave function, reaching toward the upper left and right corners. In fact, in the case of state (1,0,8) the shape of wave function is dominated by the local, rather than normal mode behavior.

C. Vibrational spectrum in the vdW energy range

In the remaining part of the bound states spectrum, within 140 cm^{-1} below dissociation threshold, we found 40 states, listed in Table III. Among these states only three are clearly assignable in terms of the normal mode quantum numbers: (8,0,0), (1,10,1), and (1,11,0). The first state is a highly excited symmetric stretch, while the two others are highly excited bending states, with little or no asymmetric stretch excitation, which explains their simplicity and localization, and is consistent with logics outlined in Sec. III B. All other well states in this energy range are assigned approximately.

At these energies, the shallow vdW plateau becomes accessible to the vibrational motion of oxygen atoms in O_3. Topologically, this part of configuration space is reached by increasing the dissociative coordinate ρ (see Figs. 3 and 4), which requires combination of asymmetric stretching and breathing motions of large-amplitudes. The usual normal modes cannot be used anymore but, for approximate assignment of the spectra, we can introduce two new effective vibration modes for the $O \cdots O_2$ complex, as shown in Fig. 8. These are *dissociative* stretching motion along ρ, described by the quantum number v_d, and "*rocking*" motion, described by the quantum number v_r. Many states listed in Table III show clear progressions of excitations of these two modes, up to $v_d = 5$ and $v_r = 6$. Note that large-amplitude rocking motion moves the system through T-shaped configuration and corresponds to highly delocalized states. The third vibration mode of the vdW complex $O \cdots O_2$ is stretching of the diatomic fragment O_2, but it remains in its ground state due to high excitation energy. So, the last column of Table III contains assignments of the vdW states in terms of (v_d, v_r).

However, since the vdW plateau is very shallow with no barrier to the covalent well, only a few vibrational states are entirely localized in the vdW range. Majority of wave functions in this energy range show non-negligible amplitudes in both the covalent well and over the vdW

TABLE III. Vibrational spectrum of ozone from energy of the vdW plateau up to dissociation threshold.

#	E, cm^{-1}	Sym.	p_w,[a] %	(v_1,v_2,v_3)[b]	(v_d,v_r)[c]
249	−139.8	A_2	29.9		(0,1)
250	−138.5	A_1	13.0		(0,0)
251	−129.9	A_2	67.7	(5,4,1)[d]	
252	−124.5	A_1	82.0	(5,5,0)[d]	
253	−103.5	A_1	57.6	(0,2,8)[d]	(1,0)
254	−102.2	A_2	15.2		(1,1)
255	−100.3	A_1	56.9	(4,1,4)[d]	(2,0)
256	−96.6	A_2	97.3	(4,5,1)[d]	
257	−88.0	A_2	99.6	(1,10,1)	
258	−85.0	A_1	90.1	(1,6,4)[d]	
259	−82.6	A_2	90.3	(2,0,7)[d]	
260	−79.9	A_1	99.8	(8,0,0)	
261	−79.1	A_1	78.9	(1,11,0)	
262	−78.7	A_1	23.9		(0,2)
263	−77.0	A_2	28.0		(2,1)
264	−74.6	A_1	25.4		(3,0)
265	−66.7	A_2	10.2		(0,3)
266	−58.7	A_2	44.3	(4,3,3)[d]	(3,1)
267	−57.0	A_1	34.3	(6,4,0)[d]	(3,0)
268	−52.1	A_1	9.2		(1,2)
269	−50.1	A_2	46.4	(5,1,3)[d]	(3,1)
270	−44.0	A_1	3.1		(0,4)
271	−42.2	A_2	19.7		(1,3)
272	−41.4	A_1	45.2	(3,3,4)[d]	(4,0)
273	−34.1	A_1	81.3	(1,1,8)[d]	
274	−33.9	A_2	40.9	(6,2,1)[d]	(4,1)
275	−29.8	A_2	78.6	(0,1,9)[d]	
276	−28.3	A_1	10.1		(2,2)
277	−23.5	A_2	4.3		(0,5)
278	−23.2	A_1	36.5	(3,8,0)[d]	(3,2)
279	−22.2	A_1	2.2		(1,4)
280	−18.8	A_2	12.3		(2,3)
281	−16.5	A_1	80.4	(0,8,4)[d]	
282	−14.0	A_2	13.2		(4,1)
283	−8.7	A_1	19.2		(5,0)
284	−8.3	A_1	1.6		(3,2)
285	−4.4	A_1	99.3	(3,0,6)[d]	
286	−2.6	A_2	10.1		(5,1)
287	−1.8	A_2	0.9		(1,5)
288	−0.4	A_1	4.1		(0,6)

[a]Probability in the covalent well.
[b]Assignment using normal-vibration modes.
[c]Assignment using vdW-type vibration modes (see text).
[d]The assignment is approximate.

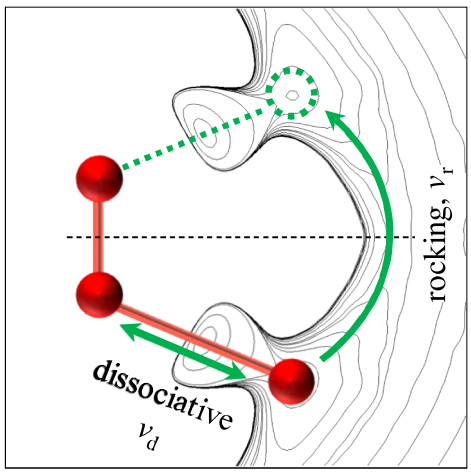

FIG. 8. Explanation of the dissociative and rocking motion local modes over the vdW plateau of the PES in O_3.

plateau. Figure 9 gives examples of wave functions for six states within 140 cm^{-1} below dissociation threshold. Three of them are almost pure vdW states, with very small amplitude in the covalent well. Three other states are mixed, showing significant amplitude everywhere. Majority of states in this energy range are like this. To quantify this point we computed, for each state in this part of spectrum, the value of probability in the covalent well ($\rho_{min} < \rho < \rho^{\ddagger}$) and included it in the fourth column of Table III, as p_w. The value of probability over the vdW plateau ($\rho^{\ddagger} < \rho < \rho_{max}$) is simply $1 - p_w$. From

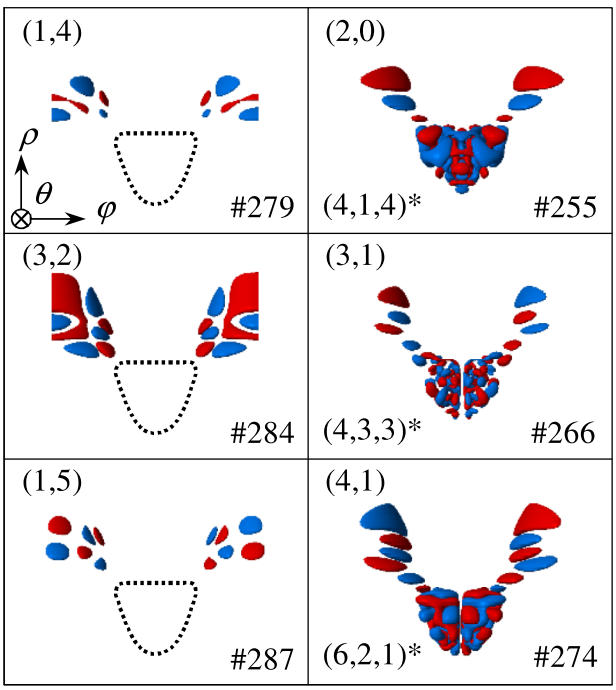

FIG. 9. Wave functions of several pure vdW states localized entirely over the plateau (left column) and several mixed states delocalized between the covalent well and the vdW plateau (right column). Assignments are given only for the vdW parts of wave functions in terms of the dissociative and rocking modes. For pure vdW states the region of the covalent well is indicated by the dashed line, for clarity.

these data one can see that there are 20 bound states, 10 of each symmetry, with probability over the vdW plateau above 66%, but only 6 states with vdW probability over 95%. All those are found within 50 cm^{-1} below dissociation threshold, and include from four to six quanta of excitations: (0,4), (0,5), (1,4), (3,2), (1,5), and (0,6).

Also note that there are two vdW plateaus in the range $2\pi/3 \le \varphi \le 4\pi/3$ (see Fig. 9), that correspond to dissociation of each bond in O_3, either $O\cdots OO$ or $OO\cdots O$. If the covalent well would not be there, one would expect to see a spectrum of the double-well system (somewhat similar to the inversion states in NH_3), namely, two sets of the rocking states, symmetric and asymmetric (A_1 and A_2), nearly degenerate at low energy and non-degenerate at higher energy. Indeed, the data presented in Table III show some of these features, but they are not particularly clear due to strong mixing with states of the deep covalent well. For example, the first two states of the (v_d, v_r) progression are (0,0) and (0,1) of symmetries A_1 and A_2. They are only 1.3 cm^{-1} apart, but this difference does not really reflect the splitting, because the state (0,1) appears at lower energy compared to (0,0), while the opposite is expected for the pure double-well system. The reason for this switch becomes obvious if one looks at the values of p_w for these (dominantly) vdW states. It appears that both have significant population in the covalent well, and more so for the state (0,1), which lowers its energy compared to the (0,0) state. As excitation of the rocking mode increases, the splitting increases. It is 12 cm^{-1} for states (0,2) and (0,3), and grows to 20.4 cm^{-1} for states (0,4) and (0,5). Similarly, this splitting is 1.3 cm^{-1} for states (1,0) and (1,1), grows to 9.9 cm^{-1} for states (1,2) and (1,3), and finally to 20.3 cm^{-1} for states (1,4) and (1,5). Also, the splitting is 9.4 cm^{-1} for states (2,2) and (2,3). These numbers seem to be consistent.

However, many splittings are off this order. Thus, states (2,0) and (2,1) are split by too much, and this is because (2,1) is an almost pure vdW state, while (2,0) is strongly mixed with (4,1,4) state in the covalent well. Similarly, states (3,0) and (3,1) are split by a lot, and this is again because (3,0) is an almost pure vdW state, while (3,1) is strongly mixed with (5,1,3) state in the covalent well. Finally, vdW states (4,0) and (4,1) are split by a lot, because both of them are strongly mixed with states in the covalent well, (3,3,4) and (6,2,1), respectively. However, states (5,0) and (5,1) are almost pure vdW states, and, as expected, are split by only 5 cm^{-1}.

One other complication is that some vdW states may show up several times in the spectrum, due to mixing with several different states of the covalent well. For example, we see from Table III that the vdW state (3,1) is found at −58.7 cm^{-1} mixed with the covalent state (4,3,3), and also at −50.1 cm^{-1} mixed with the covalent state (5,1,3). Similar behavior is found for states (3,0), (3,2), and (4,1).

Interestingly, many seemingly complicated features of the spectrum in the vdW plateau can be rationalized by analysis of two-dimensional energies ε_m^n as shown in Fig. 10, separately for symmetries A_1 and A_2. Note that in the vdW plateau range, and asymptotically, the symmetric solutions correspond to $m = 0, 2, 4, 6$, etc., while asymmetric ones correspond to $m = 1, 3, 5, 7$, etc. Although the PES itself has

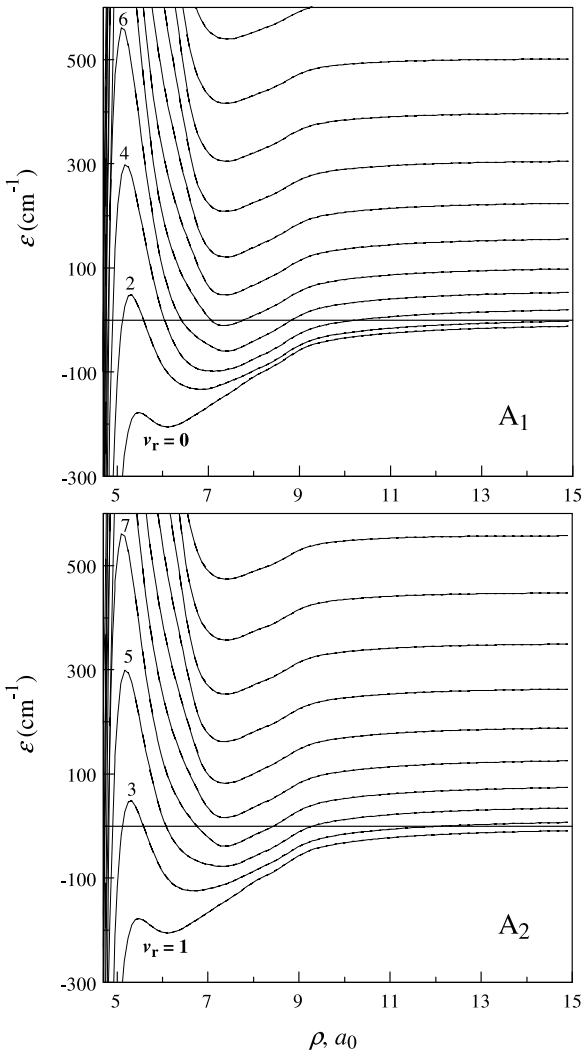

FIG. 10. Energies $\varepsilon_m(\rho)$ of two-dimensional eigenstates in the region of vdW plateau for symmetric (upper frame) and anti-symmetric (lower frame) states. Four lower energy curves in each case are labelled by the number of rocking-mode quanta, since $v_r = m$ in the plateau region. Energies at stationary points of each curve are listed in Table IV.

TABLE IV. Properties of adiabatic 1D potentials for different channels in Fig. 10.

m	ε_{min},[a] cm^{-1}	$\varepsilon^{\ddagger}$,[b] cm^{-1}	$\Delta\varepsilon$,[c] cm^{-1}
0	−204.91	−175.29[d]	29.62
1	−204.89	−175.29[d]	29.60
2	−133.2	52.4	185.7
3	−123.9	52.4	176.4
4	−98.0	296.6	394.6
5	−77.8	296.6	374.4
6	−60.4	565.9	626.3
7	−39.4	565.9	605.3

[a]Energy of the vdW minimum for the channel.
[b]Energy of the barrier top for the channel.
[c]Height of the barrier relative to the vdW minimum.
[d]Indicates a submerged reef.

no barrier between the covalent well and the vdW plateau, the $\varepsilon_m(\rho)$ dependencies all show some barrier-like features. In the case of the ground state (ε_0 for symmetric and ε_1 for asymmetric cases) we only see a tiny "reef" submerged below the dissociation asymptote, but for all upper states the top of the barrier is well above the dissociation limit. These properties are summarized in Table IV, and we see that in the cases of $m = 4$ and 5 the barrier is ~300 cm^{-1} above the dissociation limit.

It is important to understand that the value of m here is equivalent to the number of the rocking mode quanta $v_r = 6$, simply because ε_m is 2D energy, and in this part of configuration space one vibrational mode is unexcited (O_2 stretch in the O···OO complex), so, only one mode remains, which is the rocking motion. Thus, in the vdW range we can set $m = v_r$. To emphasize this point, in Fig. 10 we labelled $\varepsilon(\rho)$ dependencies using v_r, rather than m.

This, first of all, explains the appearance of the barriers in $\varepsilon(\rho)$ dependencies of Fig. 10. Indeed, even if there is no barrier along the minimum energy path on the PES, the transition state region is still very tight, and the rocking motion there (roughly normal to the dissociation coordinate) requires a lot of energy, but further in the vdW range less energy is required, which manifests as a barrier along the one-dimensional $\varepsilon_{v_r}(\rho)$ dependence.

Second, it allows to understand the spectrum of modes (v_d, v_r) over the vdW plateau using the adiabatic approximation discussed in Sec. II. According to it, the dissociation-mode states v_d could be obtained by solving one-dimensional Schrödinger equation along ρ for each potential energy curve $\varepsilon_{v_r}(\rho)$, independently. Now look at Fig. 10 (say upper frame, the symmetric case). The ground rocking state curve $v_r = 0$ has only a tiny well, separated from the covalent well by a tiny reef. This structure can support only one dissociation-mode state localized over the vdW plateau, $v_d = 0$, while all the excited states are forced to go over the reef and mix with states of the covalent well. However, the excited rocking state curve $v_r = 2$ exhibits a much more pronounced vdW well, better separated (by the barrier) from the covalent well. It can support three states of the dissociation-mode: $v_d = 0$, 1, and 2, that are localized dominantly over the vdW plateau. Similarly, the second excited rocking state curve $v_r = 4$ supports two bound states (below dissociation threshold): $v_d = 0$ and 1, while the third excited rocking state curve $v_r = 6$ supports one bound state $v_d = 0$. Overall, these considerations predict that the states (0,0), (0,2), (1,2), (2,2), (0,4), (1,4), and (0,6) are expected to be localized over the vdW plateau, while the states (1,0), (2,0), (3,0) etc. are expected to be delocalized over the vdW plateau and the covalent well (the mixed states). This simplified picture is very much consistent with exact results (and their qualitative assignments) presented in Table III. The asymmetric case (lower frame in Fig. 10) is analyzed in a similar way.

Trying to derive some simple but quantitative measure of the vdW spectrum of ozone we fitted by the Dunham expansion some of the states of the two-dimensional progression (v_d, v_r). We did not include the ground rocking states, $v_r = 0$ or 1, because, when $v_d = 0$ they require parameters very different from the other states, whereas when $v_d > 0$ they mix with covalent well states. Roughly, we can say that for majority of the vdW states $\omega_d \approx \omega_r \approx 20$ cm^{-1}, with uncertainty

within 2 cm^{-1}. However, for fundamental transition of the dissociative mode, the frequency is much higher, on the order of $\omega_d \approx 35 - 40$ cm^{-1}. This is clear from Fig. 10, where we see that the ground state curve is much tighter, compared to the excited state curves.

Finally, it should be noted that analysis of vibrational states in the vdW plateau could employ Jacobi coordinates and the corresponding set of quantum numbers, as one alternative to the assignment we devised above. In such approach the rotation of a diatomic fragment with respect to the third oxygen atom in the O···OO complex (the internal or pseudo-rotation), described by the rotational quantum number j, would replace the "rocking" mode that we used above. The other two modes would be very similar. This way of wave function assignment would be ideal asymptotically, but the potential energy map in Fig. 8 shows clearly that the PES of O_3 in the vdW region does not correspond to a free rotor (not yet). It has a shape along this delocalized vibration mode, and this shape is a double-well. For this reason, several pairs of lower energy vdW states are nearly degenerate (small splittings, as discussed above), which cannot be described by a rotational-like progression $B\,j(j+1)$. However, if we only look at the upper vdW states (excluding $v_r = 0$ or 1, just as in the previous paragraph), rename the label v_r by j in Table III, and try to fit the spectrum by

$$E(v_d, j) = \omega_d\,(v_d + \tfrac{1}{2}) - \Delta\,(v_d + \tfrac{1}{2})^2 + B\,j(j+1), \quad (27)$$

we see a reasonable fit, with standard deviation of about 2 cm^{-1}. The values $\omega_d \approx 25$ cm^{-1} and $B \approx 2.2$ cm^{-1} are obtained. So, the free-rotor picture can probably be used for upper vdW states, while for lower vdW states the picture of rocking motion through the double-well potential is more appropriate.

IV. CONCLUSIONS

In this paper we presented a method for calculation of rotational-vibrational states of triatomic molecules up to dissociation threshold (bound states) and even above (scattering resonances). The three major components of our approach are adiabatically adjusting hyper-spherical coordinates, the sequential diagonalization-truncation procedure (for the bound-like degrees of freedom), and the variable step-size grid (DVR, for the dissociative coordinate) optimized to the shape of the minimum-energy path on the potential energy surface. Calculations of resonance widths are possible by adding, at the last step of calculations, the complex absorbing potential to the asymptotic range of the PES. In this way the eigenvalue problem is solved for 3D-vibrations, without invoking the scattering formalism (such as coupled-channel). This approach is numerically efficient and allows rigorous incorporation of molecular symmetry.

New parallel code was written and used to compute energies and wave functions of the bound states of ozone, using two different potential energy surfaces: the older surface of Schinke and the newer surface of Dawes. In both cases very good agreement is obtained for all states assigned by these other authors in terms of the normal mode quantum numbers, which includes 185 lower energy states on the surface of Schinke, and 120 lower energy states on the surface of Dawes. Thus, we conclude that the theory is correct and the code is functional.

Our focus was on the upper part of vibrational spectrum, within 600 cm^{-1} below dissociation threshold (note that the covalent well of ozone is about 10 000 cm^{-1} deep). Interestingly, we found that progressions of the *symmetric-stretching* states (up to 8 quanta), and even more so of the *bending* states (up to 11 quanta), survive up to dissociation threshold and even above it, and are easy to recognize, assign, and fit reasonably well by a simple formula, such as Dunham's expansion. In contrast to this behavior, excitations of the *asymmetric-stretching* overtones tend to explore more remote parts of the PES that correlate with dissociation channels. There, wave functions of O_3 are better described by the local vibration modes (rather than normal modes), which makes the assignments problematic and accurate fitting of energies impossible.

Finally, within 140 cm^{-1} below dissociation threshold, a broad plateau on the PES becomes accessible by large-amplitude vibrations of a floppy van der Waals type complex O···O_2. In this energy range the spectrum of ozone can be assigned quantum numbers using a two-dimensional progression of the vibration modes: the *rocking-motion* states, and the *dissociative-motion* states, up to 6 quanta in each, both with very low frequency on the order of 20 cm^{-1}. However, fundamental excitations of the ground rocking states require higher frequencies, about 35 and 40 cm^{-1} (depending on state symmetry), due to large anharmonicity brought about by the double-well character of the PES near dissociation. Many of these (van der Waals plateau) states are mixed with the normal mode states of the main (covalent) well and, thus, are delocalized over a very large part of configuration space. Interestingly, we found that excitation of the rocking-motion helps to keep van der Waals states localized within the plateau region, by raising the *effective barrier*, even though the PES itself has no barrier between the covalent well and the van der Waals plateau.

Several improvements and further developments of the method are possible. First, the rigorous treatment of permutation group S_3 in calculations with $J > 0$ requires vibrational states of E-symmetry (doubly degenerate), in addition to symmetries A_1 and A_2 considered here. These states can be easily obtained by expanding the grid for hyper-angle φ onto its full physical range: $0 \le \varphi \le 2\pi$. Such calculations are ongoing and will be reported elsewhere.

Another improvement could be a better treatment of singularity along the equator of the hypersphere, $\theta = \pi/2$. Here we just checked and found that since this singularity is very narrow, and the DVR points are placed at the middle of the intervals (rather than at their borders), the effect of this singularity is minimal: it only affects, by ~2 cm^{-1}, energies of the upper 17 most-delocalized states, which can be mediated by choosing carefully the value of θ_{max} (slightly smaller than $\pi/2$). More rigorous and automated treatments of singularities are known[58] and could be incorporated into our method.

Lastly, it should be admitted that the present formulation employs the centrifugal-sudden assumption, and thus is approximate for $J > 0$ states. More rigorous inclusion of the ro-vibrational coupling effect, due to the Coriolis term of Eq. (3), is desirable. In the future we plan testing the role of Coriolis effect in O_3 by including couplings between some (e.g., the nearest) K-blocks of the overall Hamiltonian matrix for $J > 0$.

Understanding the vibrational states of O_3 in the window 600 cm^{-1} below dissociation threshold is important because, as we showed in our recent paper,[11] this part of the vibrational spectrum plays the most important role in the recombination process that forms ozone. Due to rotation of O_3 molecules at thermal energies (up to $J \sim 40$), these bound states are lifted by the centrifugal potential to energies above dissociation threshold, which makes them *scattering resonances* O_3^* that can receive population from continuum through collisions, $O + O_2 \rightarrow O_3^*$, and can contribute to ozone formation. We think that a moderate centrifugal lift (say $J \sim 20$–30) causes only a slight change of wave functions for many of these states, due to their very significant vibrational content and distinct modal structure. Thus, understanding the highly excited vibrational states in non-rotating O_3 ($J = 0$) should be helpful in the future for analysis and assignment of wave functions of the rotationally excited states ($J > 0$).

SUPPLEMENTARY MATERIAL

See the supplementary material for the complete vibrational spectrum of ozone up to −600 cm^{-1}, Table S-I.

ACKNOWLEDGMENTS

Richard Dawes is gratefully acknowledged for sharing his new PES of ozone. This research was supported by the NSF Atmospheric Chemistry Program, Division of Atmospheric Sciences, Grant No. AGS-1252486. This research used resources of the National Energy Research Scientific Computing Center, which is supported by the Office of Science of the U.S. Department of Energy under Contract No. DE-AC02-05CH11231. Alexander Teplukhin acknowledges support from Arthur J. Schmitt Leadership Fellowship.

APPENDIX: ASYMPTOTIC FORM OF TWO-DIMENSIONAL EIGENSTATES

Here we show that asymptotically, as $\rho \rightarrow \infty$, a solution of two-dimensional Schrödinger equation with Hamiltonian operator $\hat{h}_n$ acting on wave function $\Lambda(r,\Theta)$ can be obtained analytically. To recap, the operator $\hat{h} = \hat{T}_{\theta\varphi} + V_{ext} + V_{sym} + V_{pot}$ has four components (omitting index n),

$$\begin{aligned} \hat{T}_{\theta\varphi} &= -\frac{\hbar^2}{2\mu}\cdot\frac{4}{\rho^2}\left(\frac{\partial^2}{\partial\theta^2}+\frac{1}{\sin^2\theta}\frac{\partial^2}{\partial\varphi^2}\right), \\ \hat{V}_{ext} &= -\frac{\hbar^2}{2\mu}\cdot\frac{1}{\rho^2}\left(\frac{1}{4}+\frac{4}{\sin^2 2\theta}\right), \\ V_{sym} &= \bar{A}\hbar^2 J(J+1)+(C-\bar{A})\hbar^2 K^2, \end{aligned} \tag{A1}$$

and the potential energy surface $V_{pot} = V_{pot}(\rho,\theta,\varphi)$. To find the asymptotic form of the operator, it is convenient to transform all four components from the APH coordinates (ρ,θ,φ) to mass-scaled Jacobi coordinates (S,s,Θ) and then consider a limit $S \rightarrow \infty$. We start with the following transformation:[18]

$$\begin{aligned} S &= \frac{\rho}{\sqrt{2}}(1+\sin\theta\cos\varphi)^{1/2}, \\ s &= \frac{\rho}{\sqrt{2}}(1-\sin\theta\cos\varphi)^{1/2}, \\ \cos\Theta &= \frac{\sin\theta\sin\varphi}{\left(1-\sin^2\theta\cos^2\varphi\right)^{1/2}}. \end{aligned} \tag{A2}$$

The first component, $\hat{T}_{\theta\varphi}$ transforms as follows:

$$\begin{aligned} \frac{4}{\rho^2}\left(\frac{\partial^2}{\partial\theta^2}+\frac{1}{\sin^2\theta}\frac{\partial^2}{\partial\varphi^2}\right) &= \frac{1}{S^2+s^2}\left(s^2\frac{\partial^2}{\partial S^2}-2Ss\frac{\partial^2}{\partial S\partial s}+S^2\frac{\partial^2}{\partial s^2}\right)-\left(\frac{S^2}{S^2+s^2}+\frac{S^4-s^4}{S^4+s^4-(2Ss\sin\Theta)^2}\right)\frac{1}{S}\frac{\partial}{\partial S} \\ &\quad -\left(\frac{s^2}{S^2+s^2}-\frac{S^4-s^4}{S^4+s^4-(2Ss\sin\Theta)^2}\right)\frac{1}{s}\frac{\partial}{\partial s}+\frac{S^2+s^2}{(Ss)^2}\frac{\partial^2}{\partial\Theta^2}-\frac{2\sin 2\Theta(S^2+s^2)}{S^4+s^4-(2Ss\sin\Theta)^2}\frac{\partial}{\partial\Theta}. \end{aligned} \tag{A3}$$

The second component $\hat{V}_{ext}$ transforms as follows:

$$\frac{1}{\rho^2}\left(\frac{1}{4}+\frac{4}{\sin^2 2\theta}\right) = \frac{1}{4(S^2+s^2)}+\frac{(S^2+s^2)^3}{(2Ss\sin\Theta)^2(S^4+s^4-(2Ss\sin\Theta)^2)}. \tag{A4}$$

In the limit $S \rightarrow \infty$, many terms in these two components vanish and their sum approaches the following expression, that depends on s and Θ only:

$$\left(-\frac{\hbar^2}{2\mu}\right)^{-1}\lim_{S\rightarrow\infty}(T_{\theta\varphi}+V_{ext}) = \frac{\partial^2}{\partial s^2}+\frac{1}{s}\frac{\partial}{\partial s}+\frac{1}{s^2}\frac{\partial^2}{\partial\Theta^2}+\frac{1}{4s^2\sin^2\Theta} = \left(\frac{\partial^2}{\partial s^2}+\frac{1}{s}\frac{\partial}{\partial s}-\frac{1}{4s^2}\right)+\frac{1}{s^2}\left(\frac{\partial^2}{\partial\Theta^2}+\frac{1}{4\sin^2\Theta}+\frac{1}{4}\right). \tag{A5}$$

A similar expression was reported by Billing.[36] Now we transform to non-scaled Jacobi coordinates that include interatomic distance r (instead of s) and the reduced mass of O_2 (instead that of O_3),

$$\lim_{S\to\infty}(T_{\theta\varphi}+V_{ext}) = \left(-\frac{\hbar^2}{2\mu_{O_2}}\right)\left(\frac{\partial^2}{\partial r^2}+\frac{1}{r}\frac{\partial}{\partial r}-\frac{1}{4r^2}\right) + \left(-\frac{\hbar^2}{2\mu_{O_2}r^2}\right)\left(\frac{\partial^2}{\partial\Theta^2}+\frac{1}{4\sin^2\Theta}+\frac{1}{4}\right). \quad \text{(A6)}$$

To simplify this part of the operator $\hat{h}$, we transform the initial wave function $\Lambda(r,\Theta)$ to a new wave function $\tilde{\Lambda}(r,\Theta)$,

$$\tilde{\Lambda}(r,\Theta) = \sqrt{\frac{r}{\sin\Theta}}\Lambda(r,\Theta). \quad \text{(A7)}$$

This transformation eliminates all terms except the two second derivatives

$$\tilde{h} = -\frac{\hbar^2}{2\mu_{O_2}}\frac{\partial^2}{\partial r^2} - \frac{\hbar^2}{2\mu_{O_2}r^2}\frac{1}{\sin\Theta}\frac{\partial}{\partial\Theta}\sin\Theta\frac{\partial}{\partial\Theta}. \quad \text{(A8)}$$

Finally, we assume asymptotic form of rotational potential $V_{sym} = \hbar^2K^2/(2\mu_{O_2}r^2\sin^2\Theta)$, as discussed in Sec. II B, and asymptotic form of potential energy surface, which is simply a potential energy of O_2 fragment, i.e., $V_{pot} \to V_{O_2}(r)$,

$$\tilde{h} = -\frac{\hbar^2}{2\mu_{O_2}}\frac{\partial^2}{\partial r^2} - \frac{\hbar^2}{2\mu_{O_2}r^2} \times\left(\frac{1}{\sin\Theta}\frac{\partial}{\partial\Theta}\sin\Theta\frac{\partial}{\partial\Theta}-\frac{K^2}{\sin^2\Theta}\right)+V_{O_2}(r). \quad \text{(A9)}$$

Now, we approximate the wave function as $\tilde{\Lambda}(r,\Theta) = R(r)\cdot A(\Theta)$ and note that the action of angular operator (in parenthesis) could be expressed using its eigenvalues $j(j+1)$ and associated Legendre polynomials $A(\Theta) = P_j^K(\Theta)$, namely,

$$\left(-\frac{1}{\sin\Theta}\frac{\partial}{\partial\Theta}\sin\Theta\frac{\partial}{\partial\Theta}+\frac{K^2}{\sin^2\Theta}\right)P_j^K(\Theta) = j(j+1)P_j^K(\Theta), \quad j\geq K. \quad \text{(A10)}$$

This reduces the initial two-dimensional Schrödinger equation to a set of one-dimensional Schrödinger equations $\tilde{h}^j R_v^j(r) = \varepsilon_{v,j}R_v^j(r)$ for vibrational coordinate r and for different values of the angular momentum quantum number j of the diatomic fragment that sets up the centrifugal potential of the diatomic product

$$\tilde{h}^j = -\frac{\hbar^2}{2\mu_{O_2}}\frac{\partial^2}{\partial r^2}+\frac{j(j+1)\hbar^2}{2\mu_{O_2}r^2}+V_{O_2}(r), \quad j\geq K. \quad \text{(A11)}$$

For a given value of the vibrational quantum number v (for example, $v=0$) energies $\varepsilon_{v,j}$ constitute a *non-degenerate* rotational spectrum $j(j+1)$ of a rigid rotor, that starts with a quantum number $j=K$. If one neglects the effects of potential anharmonicity and centrifugal distortion, then energies $\varepsilon_{v,j}$ could be estimated as

$$\varepsilon_{v,j} \approx \hbar\omega\left(v+\tfrac{1}{2}\right)+\frac{j(j+1)\hbar^2}{2\mu r_0^2}, \quad j\geq K. \quad \text{(A12)}$$

In this expression, ω and r_0 are vibrational frequency and equilibrium interatomic distance of oxygen molecule, respectively. Indeed, this solution is consistent with density of points in the rightmost slice in Fig. 3. Two vibrational levels $v=0$ and $v=1$ are easily recognizable, and the spacing between rotational levels in $v=0$ is increasing with energy. The ground state $v=0$, $j=0$ located at $\varepsilon_{0,0} = 791.63$ cm^{-1} above asymptotic limit of the potential energy surface is forbidden by symmetry. So, the first allowed state is $v=0$, $j=1$ with energy $\varepsilon_{0,1} = 794.51$ cm^{-1}.

[1] X. Wang, S. Carter, and J. M. Bowman, J. Phys. Chem. A **119**, 11632 (2015).
[2] Y. Wang and J. M. Bowman, J. Phys. Chem. Lett. **6**, 124 (2015).
[3] J. Li, S. Carter, J. M. Bowman, R. Dawes, D. Xie, and H. Guo, J. Phys. Chem. Lett. **5**, 2364 (2014).
[4] R. Dawes, X. G. Wang, and T. Carrington, J. Phys. Chem. A **117**, 7612 (2013).
[5] P. Jankowski, G. Murdachaew, R. Bukowski, O. Akin-Ojo, C. Leforestier, and K. Szalewicz, J. Phys. Chem. A **119**, 2940 (2015).
[6] R. Dawes, P. Lolur, A. Li, B. Jiang, and H. Guo, J. Chem. Phys. **139**, 201103 (2013).
[7] Y. Li, Z. Sun, B. Jiang, D. Xie, R. Dawes, and H. Guo, J. Chem. Phys. **141**, 81102 (2014).
[8] Z. Sun, D. Yu, W. Xie, J. Hou, R. Dawes, and H. Guo, J. Chem. Phys. **142**, 174312 (2015).
[9] T. R. Rao, G. Guillon, S. Mahapatra, and P. Honvault, J. Phys. Chem. Lett. **6**, 633 (2015).
[10] T. Rajagopala Rao, G. Guillon, S. Mahapatra, and P. Honvault, J. Chem. Phys. **142**, 174311 (2015).
[11] A. Teplukhin and D. Babikov, Phys. Chem. Chem. Phys. **18**, 19194 (2016).
[12] W. Xie, L. Liu, Z. Sun, H. Guo, and R. Dawes, J. Chem. Phys. **142**, 64308 (2015).
[13] J. Crawford and G. A. Parker, J. Chem. Phys. **138**, 54313 (2013).
[14] M. Lara, A. Aguado, M. Paniagua, and O. Roncero, J. Chem. Phys. **113**, 1781 (2000).
[15] D. Babikov and B. K. Kendrick, J. Chem. Phys. **133**, 174310 (2010).
[16] J. Blandon and V. Kokoouline, Phys. Rev. Lett. **102**, 143002 (2009).
[17] B. Kendrick and R. T Pack, J. Chem. Phys. **104**, 7475 (1996).
[18] R. T Pack and G. A. Parker, J. Chem. Phys. **87**, 3888 (1987).
[19] A. Teplukhin and D. Babikov, Chem. Phys. Lett. **614**, 99 (2014).
[20] J. S. Francisco, J. R. Lyons, and I. H. Williams, J. Chem. Phys. **123**, 54302 (2005).
[21] K. A. Peterson, J. R. Lyons, and J. S. Francisco, J. Chem. Phys. **125**, 84314 (2006).
[22] G. B. Ma, R. Q. Chen, and H. Guo, J. Chem. Phys. **110**, 8408 (1999).
[23] L. S. Cederbaum, P. Stampfuû, and W. Wenzel, Chem. Phys. **259**, 211 (2000).
[24] X. Huang, D. W. Schwenke, S. A. Tashkun, and T. J. Lee, J. Chem. Phys. **136**, 124311 (2012).
[25] B. R. Johnson, J. Chem. Phys. **79**, 1916 (1983).
[26] A. Kuppermann, Chem. Phys. Lett. **32**, 374 (1975).
[27] D. Babikov, B. K. Kendrick, R. B. Walker, R. T Pack, P. Fleurat-Lesard, and R. Schinke, J. Chem. Phys. **118**, 6298 (2003).
[28] V. Kokoouline and C. H. Greene, Phys. Rev. A **69**, 32711 (2004).
[29] V. Kokoouline, C. H. Greene, and B. D. Esry, Nature **412**, 891 (2001).
[30] V. Kokoouline and C. H. Greene, Phys. Rev. A **68**, 12703 (2003).
[31] B. Yang, W. Chen, and B. Poirier, J. Chem. Phys. **135**, 94306 (2011).
[32] H. Suno, J. Chem. Phys. **135**, 134312 (2011).
[33] D. M. Leitner, J. D. Dol, and R. M. Whitnell, J. Chem. Phys. **94**, 6644 (1991).
[34] R. M. Whitnell and J. C. Light, J. Chem. Phys. **90**, 1774 (1989).
[35] M. V. Ivanov and D. Babikov, J. Chem. Phys. **134**, 144107 (2011).
[36] G. Billing, *The Quantum Classical Theory* (Oxford University Press, New York, 2003).
[37] A. Teplukhin, M. Ivanov, and D. Babikov, J. Chem. Phys. **139**, 124301 (2013).
[38] J. M. Bowman, Chem. Phys. Lett. **217**, 36 (1994).
[39] S. Y. Grebenshchikov and R. Schinke, J. Chem. Phys. **131**, 181103 (2009).
[40] S. L. Zou, S. Skokov, and J. M. Bowman, J. Phys. Chem. A **105**, 2423 (2001).
[41] J. C. Light and T. Carrington, in *Advances in Chemical Physics*, edited by I. Prigogine and S.A. Rice (John Wiley & Sons, Inc., Hoboken, NJ, USA, 2000), pp. 263–310.

[42]Z. Bačić and J. C. Light, J. Chem. Phys. **85**, 4594 (1986).
[43]J. C. Light and Z. Bačić, J. Chem. Phys. **87**, 4008 (1987).
[44]Z. Bačić and J. C. Light, J. Chem. Phys. **86**, 3065 (1987).
[45]O. I. Tolstikhin, S. Watanabe, and M. Matsuzawa, J. Phys. B: At., Mol. Opt. Phys. **29**, L389 (1996).
[46]V. Kokoouline and F. Masnou-Seeuws, Phys. Rev. A **73**, 12702 (2006).
[47]V. Kokoouline, O. Dulieu, R. Kosloff, and F. Masnou-Seeuws, J. Chem. Phys. **110**, 9865 (1999).
[48]A. G. Borisov, J. Chem. Phys. **114**, 7770 (2001).
[49]J. Blandon, V. Kokoouline, and F. Masnou-Seeuws, Phys. Rev. A **75**, 42508 (2007).
[50]M. Ayouz, O. Dulieu, R. Guérout, J. Robert, and V. Kokoouline, J. Chem. Phys. **132**, 194309 (2010).
[51]M. Ayouz, O. Dulieu, and J. Robert, J. Phys. Chem. A **117**, 9941 (2013).
[52]L. S. Blackford, J. Choi, A. Cleary, E. D'Azeuedo, J. Demmel, I. Dhillon, J. J. Dongarra, S. Hammarling, G. Henry, A. Petitet, K. Stanley, D. Walker, and R. C. Whaley, *ScaLAPACK User's Guide* (Society for Industrial and Applied Mathematics, 1997).
[53]S. Y. Grebenshchikov, R. Schinke, P. Fleurat-Lessard, and M. Joyeux, J. Chem. Phys. **119**, 6512 (2003).
[54]D. Babikov, J. Chem. Phys. **119**, 6554 (2003).
[55]H. S. Lee and J. C. Light, J. Chem. Phys. **120**, 5859 (2004).
[56]S. Ndengué, R. Dawes, X.-G. Wang, T. Carrington, Z. Sun, and H. Guo, J. Chem. Phys. **144**, 74302 (2016).
[57]R. Siebert, P. Fleurat-Lessard, R. Schinke, M. Bittererová, and S. C. Farantos, J. Chem. Phys. **116**, 9749 (2002).
[58]B. K. Kendrick, R. T Pack, R. B. Walker, and E. F. Hayes, J. Chem. Phys. **110**, 6673 (1999).